

Magnetic Fields in High Velocity Clouds and Rotation Measure Foreground Removal Techniques

Olivia Walters

Supervisors: Craig Anderson, Naomi McClure-Griffiths

An honours thesis (mid-term report) submitted for
The Australian National University
Research School of Astronomy and Astrophysics

August 2024

© Olivia Walters 2024

Draft Copy – 2 August 2024

Except where otherwise indicated, this thesis is my own original work.

Olivia Walters
2 August 2024

Acknowledgments

Who do you want to thank?

Abstract

NB: This abstract is old! It should not be looked at!

High Velocity Clouds (HVCs) are a proposed solution to how extragalactic gas enters into star-forming galaxies. However, the presence of magnetic fields is required to ensure that HVCs can travel through the halo without being torn apart by ram pressure. This report aims to measure the strength of the magnetic fields present within the Milky Way's halo and surrounding circumgalactic HVCs, to determine if they can support HVCs as they travel through the Galactic halo. This report uses data from the ASKAP Polarisation Sky Survey of the Universe's Magnetism (POSSUM) to pull a series of rotation measures (RMs) across the southern sky. These RMs are then converted into magnetic fields using an algorithm, developed using previously collected data from the Smith Cloud. Statistical analysis tools are applied to confirm if hypothesised magnetic fields can support HVCs. The report finds that [Summary of discussion and conclusion] ...

Contents

| | |
|--|------------|
| Acknowledgments | iii |
| Abstract | iv |
| 1 Introduction | 1 |
| 1.1 High Velocity Clouds | 1 |
| 1.1.1 Chemical Properites and Emission | 2 |
| 1.2 Magnetic Fields | 3 |
| 1.2.1 Draping | 3 |
| 1.2.2 Faraday Rotation | 4 |
| 1.2.2.1 Noise Interference | 5 |
| 1.3 Smith Cloud | 7 |
| 1.4 Report Outline and Objectives | 7 |
| 2 Data Collection | 10 |
| 2.1 The Australian Square Kilometer Array Pathfinder (ASKAP) | 10 |
| 2.2 Observational Data | 11 |
| 2.2.1 RM Sky Interpolation | 11 |
| 2.2.2 Other Data Sources | 12 |
| 2.3 Selection of HVCs | 12 |
| 2.4 Data Collation | 14 |
| 2.4.1 HVC Image Overlays | 14 |
| 3 Foreground Subtraction | 16 |
| 3.1 Interpolation | 16 |
| 3.2 Annulus Subtraction | 17 |
| 3.3 Fast Fourier Transforms (FFTs) | 18 |
| 3.3.1 Non-Uniform Fast Fourier Transforms (NUFFTs) | 19 |
| 3.3.2 Bandpass Filtering | 20 |
| 3.3.3 Kernel Filtering | 22 |
| 3.4 Characterising the RM data | 23 |
| 3.5 Other Methods | 26 |

| | |
|--|-----------|
| 4 Magnetic Field Derivation | 27 |
| 4.1 Assumptions | 27 |
| 4.2 Derivation of Line-of-Sight Magnetic Fields | 28 |
| 4.3 KS Testing | 30 |
| 4.4 Mathematical methods to evaluate HVC Magnetic Fields | 32 |
| 4.4.1 KS-EDF Method | 33 |
| 4.4.2 Uncertainty Subtraction | 34 |
| 4.5 Toy Model Analysis | 35 |
| 4.6 Magnetic Field Results | 35 |
| 4.6.1 Uncertainties | 37 |
| 4.6.2 Statistical Comparison of Methods | 39 |
| 5 Discussion | 40 |
| 5.1 Foreground Removal | 40 |
| 5.1.1 Edge Detection and Rippling | 40 |
| 5.1.2 Comparison of Methods | 40 |
| 5.1.3 Sample Size Limitations | 40 |
| 5.2 Magnetic Field Derivation | 40 |
| 5.2.1 Data Collection | 41 |
| 5.2.2 Necessity of Assumptions | 41 |
| 5.2.3 Validity of Derivation Methods | 41 |
| 5.2.4 Uncertainty Analysis | 41 |
| 6 Conclusions | 42 |
| 6.1 Future Research | 42 |
| Bibliography | 48 |
| Appendix | 49 |
| A Developed code and data | 49 |
| B All HVCs and HVC Calculations | 49 |
| C Planck Mission Cosmic Microwave Background | 49 |
| D PyNUFFT Python Module | 49 |

List of Figures

| | | |
|-----|--|----|
| 1.1 | From Konz et al. [2002], figure 2. An example of a typical HVC shape and structure, specifically that of HVC125+41-207. The contour lines and shading indicate HI column density. | 2 |
| 1.2 | From Loi et al. [2019], figure 4. A graph of the relationship between the sensitivity at 1.4 GHz (x-axis) and the minimum number of RM sample points per square degree (y-axis). The black points are not relevant to the report, but the purple line and equation describe the determined relationship. | 6 |
| 1.3 | From Macquart et al. [2012], figure 1. A graph displaying the effect of observational (stokes parameters) signal-to-noise ratio the resultant faraday depth on a sample set of observations. | 8 |
| 1.4 | From Lockman et al. [2008], figure 1. A HI image of the Smith Cloud taken from the Green Bank Telescope at a local standard of velocity rest of 100 kms^{-1} . The purpose of the arrows are not meaningful to this paper. | 9 |
| 2.1 | An Aitoff projection of all portions of the RM sky observed by ASKAP for the POSSUM survey. The map is up to date as of May 2024 and all RMs in this map are used in the production of this report. The faraday depth of these RMs are indicated by colour. | 11 |
| 2.2 | Cartesian plots of peripheral data maps (left): the HI sky from the Westmeier [2018] modification of the HI4PI survey (top); the H-alpha sky from Finkbeiner [2003] (middle); and the Hutschenreuter map from Hutschenreuter and Enßlin [2020]; Hutschenreuter et al. [2022] (bottom). Uncertainty maps for H-alpha and the Hutschenreuter map are displayed respectively (right). The HI uncertainty is not displayed due to it simply being a scalar multiple of the HI map. | 13 |
| 2.3 | (Left) A graph of all ~ 180000 RMs plotted against their corresponding galactic latitude; (Right) The corresponding graph of all interpolated faraday depths matched to the POSSUM RMs. Both graphs represent a significant level of scatter present in RMs collected near the galactic midplane. | 15 |

| | | |
|-----|---|----|
| 3.1 | An Aitoff projection of all portions of the RM sky observed by ASKAP for the POSSUM survey similar to 2.1, filtered through a proprietary fixed-sampling algorithm with inner radius of 0.4" and a sampling constant of 50. | 18 |
| 3.2 | (Right) A cropped and grayscale image of the CMB. (Left) The same image after being fed through a forward then adjoint NUFFT. The amount of sample points total to 27000. Both plots share a common intensity colourbar for reference. | 20 |
| 3.3 | Crosshatch-Bandpassed versions of the interpolated RM sky at various opacity gradings - where "original" means 0% opacity. The term "opacity" refers to the effect of the bandpass e.g. 100% opacity means the bandpass completely removes selected frequencies and 50% opacity means that the bandpass halves the presence of selected frequencies. . . . | 21 |
| 3.4 | Cartesian plots of the interpolated RM sky (Top) compared against the Annulus-Bandpassed version of the interpolated RM sky (Bottom). The annulus kernel used sums to unity, making it act like a unitary operator, standard for blurring techniques [Pulfer, 2019]. | 22 |
| 3.5 | Residual histogram plots of the actual POSSUM RMs compared to the corresponding various foreground removal methods: interpolation (Top left); crosshatch-bandpassed (Top right); annulus-bandpassed (Bottom left); and annulus-convolved (Bottom right). | 24 |
| 3.6 | Three corner plots of all RM sampling points, describing the relationship between the several associated RM values and Galactic latitude indicated by colour. (Top left) a comparison between actual RMs, interpolated RMs, and Crosshatch-Bandpassed RMs. (Top right) a comparison between actual RMs, interpolated RMs, and Annulus-Convolved RMs. (Bottom) a comparison between actual RMs, Annulus-Bandpassed RMs, and Annulus-Convolved RMs. | 25 |
| 4.1 | All 14 HVCs used in the analysis of the primary outcome. The HI column density is represented using a grayscale image background. The RMs are represented by circular markers, their size equal to the magnitude and the colour representative of their sign with Red being positive. The black circle is the maximum-extent HVC area and the black 'x' indicates the centre of the HVC. | 29 |
| 4.2 | Two histograms describing the calculated line-of-sight virtual magnetic field strengths within a certain distance to the 14 sample HVCs. The red histogram uses uncorrected. The green histogram uses corrected RMs. | 31 |

| | | |
|-----|---|----|
| 4.3 | A diagram representing the physical evaluation of the KS-EDF method. The graph shows the EDFs of inside and outside populations for an example HVC. The lines drawn on the diagram represent the statistic value and the KS-EDF magnetic field value. | 33 |
| 4.4 | A boxplot representing the absolute-value magnetic field of each HVC for both derivational methods. The red and blue dotted lines indicate two upper bounds, one set by the Grønnow et al., simulations, and the other by the Smith Cloud respectively. | 37 |
| 4.5 | A graph displaying the relationship between the absolute GSR velocity and the absolute magnetic field for each corresponding HVC. Lines of fit for the two methods used are displayed as well. | 38 |

List of Tables

| | | |
|-----|--|----|
| 4.1 | A table describing the KS test results for each HVC. | 32 |
| 4.2 | A table describing the magnetic field derivations for each HVC. HVCs from the sample of 14 that had no significant KS test detection, or an invalid variance subtraction result are removed. | 36 |
| 4.3 | A table describing the linear fit model parameters of the relationship described in equation 4.8 and displayed in figure 4.5. | 37 |

Introduction

The question of how gas is accreted into galaxies fuelling star-formation is a puzzle that has perplexed Astronomers for decades. Due to the complexities in the structures of star-forming galaxies, there are many factors involved in the process of, and potential sources of accretion. What Astronomers do know, at least, is that star-forming galaxies require a continuous supply of fresh gas to continue their star formation.

Due to observational constraints, Astronomers are required to attempt to answer this question by examining the behaviours of our own Milky Way and Local Group environment, assuming the Milky Way is typical of a star-forming galaxy.

A major factor to consider when answering this question is where fresh pristine gas comes from, and by what mechanism it takes to enter the disks of star-forming galaxies. High Velocity Clouds (HVCs) have been a suggested mechanism for Galactic gas accretion and this report aims to evaluate the viability of this suggestion.

1.1 High Velocity Clouds

HVCs are clouds of gas found in the Milky Way's Circumgalactic Medium (CGM) and Galactic halo and are notable primarily for their high peculiar velocity relative to the Galactic Standard of Rest (GSR), typically $70\text{-}90 \text{ kms}^{-1}$ [Wakker, 1991; Wakker and van Woerden, 1997; Blitz et al., 1999]. As will be shown in section 1.2.1, this increased speed, and its interaction with halo magnetic fields, is hypothesized to allow the HVC to survive as it travels through the CGM and halo so it can reach the Galactic disk and Interstellar Medium (ISM) of the Milky Way.

The origin of HVCs is still unknown, with a few hypotheses as to where they originate. Blitz et al. [1999] suggests that HVCs originate from the Intergalactic Medium (IGM) surrounding the local group. However, there is also a belief that some HVCs likely 'tore off' from satellites like the Magellanic Clouds, due to the presence of their own dark matter subhaloes, and the existence of HVCs in the Magellanic Stream and Leading Arm [Kaczmarek et al., 2017; McClure-Griffiths et al., 2010].

HVCs typically have a neutral mass gas content of $3 \times 10^7 M_\odot$ and a dark matter content of $3 \times 10^8 M_\odot$ [Blitz et al., 1999]. They are generally shaped like comets, with a primary bulb that is approximately 0.5-25 kpc in diameter - a value that is highly dependent on distance to the Galactic midplane, which can range from approx. 50



Figure 1.1: From Konz et al. [2002], figure 2. An example of a typical HVC shape and structure, specifically that of HVC125+41-207. The contour lines and shading indicate HI column density.

kpc - 1 Mpc [Blitz et al., 1999; Konz et al., 2002]. Furthermore, HVCs have tail-like structures that account for one eighth the baryonic mass of the HVC [Konz et al., 2002]. These tails leave behind long streams of gas that remain after collision with the Galactic disk [Putman et al., 2012]. This size-distance correlation, comet-like structure, and long streaming tails suggest quite conclusively that HVCs shed a lot of material as they make their journey to the ISM.

Figure 1.1 is from Konz et al. [2002], which provides a typical example of what a HVC looks like in HI, specifically using the example of HVC125+41-207.

1.1.1 Chemical Properites and Emission

HVCs have several characteristics that allow them to be both detected and analysed. Due to their hypothesised origins in extragalactic gas, HVCs contain mostly hydrogen gas such as HI, which can be seen with 21 cm emission [Wakker, 1991; Wakker and van Woerden, 1997; Westmeier, 2018]. The proportion of ionised gas in HVCs is still heavily debated. HVCs also typically contain molecular gas that emits H-alpha, however due to extinction effects, it is difficult to observe H-alpha emission correctly [Bland-Hawthorn and Maloney, 1999; Finkbeiner, 2003]. Another difficulty for H-alpha analysis is that HVCs typically do not contain CO in significant quantities, CO a common tracer for H-alpha [Blitz et al., 1999].

Despite HVCs supposed gas purity, there is evidence that HVCs can contain alpha group elements. Hill et al. [2009]; Madsen et al. [2006] found the presence of [NII] 6583Å, [SII] 6716Å, and [OIII] 5007Å emission lines – with a conclusion that Nitrogen abundance is 0.15-0.44 times solar abundance levels. The observation of these emission lines can help constrain the metallicity of any HVC [Hill et al., 2009]. Metallicity

is important in both answering the capacity for HVCs to supply fresh gas for star formation, and the mechanism by which HVCs can survive [Grønnow et al., 2018]; more on the latter in section 1.2.1. While HVCs can contain heavier elements Hayakawa and Fukui [2024] finds that these concentrations are low enough that HVCs can remain as viable candidates for fuelling star formation via gas accretion.

HVCs additionally have a temperature relationship with proximity to the Galactic midplane, with an average HVC temperature of 10000 K and a range of temperatures ranging from 8000 – 12000 K [Hill et al., 2009; Madsen et al., 2006]. The temperature of a HVC is in the region in which atomic hydrogen transitions from neutral (HI) to ionised (HII), suggesting that HVCs may be partly ionised [Hill et al., 2009; Madsen et al., 2006; Kawaguchi, 1952]. This temperature relationship is dependent on their position with respect to the Galactic midplane, with HVCs closer to the midplane generally being cooler [Madsen et al., 2006].

1.2 Magnetic Fields

The primary issue facing HVCs as an explanation for gas accretion is its capacity to survive as it travels through the CGM and Galactic halo. As discussed, in section 1.1, HVCs can lose a lot of size and mass as it approaches towards the Galactic disk, with the long trails it leaves behind being evidence for ram-pressure stripping as the HVC collides with the gas present in the halo [Jones et al., 1996; Grønnow et al., 2017, 2022]. Heitsch and Putman [2009] demonstrates that without anything to counter this effect, HVCs with masses under $10^{4.5} M_{\odot}$ would completely disperse within 10 kpc of halo travel.

Additionally, HVCs are subject to Kelvin-Helmholtz (K-H) instabilities, which is triggered by the nature of the HVC being a cloud of warm gas travelling at high speeds through a medium. These K-H instabilities are a significant factor that would lead a to HVC collapsing before it reaches the Galactic disk [Jones et al., 1996; Grønnow et al., 2017, 2022].

1.2.1 Draping

The proposed solution to handle this problem is magnetic fields. The Galactic halo is magnetised to some degree in a generally turbulent manner [Mao et al., 2010; Han and Qiao, 1994; Jung et al., 2023; Beck et al., 2012]. It is hypothesised that HVCs accumulate these existing magnetic fields in the Galactic halo, causing them to cloak the HVC with a shield that protects against ram pressure stripping and suppresses K-H instabilities [Dursi and Pfrommer, 2008; Jones et al., 1996; Konz et al., 2002; Grønnow et al., 2017, 2018; Jung et al., 2022]. This phenomenon is referred to as 'magnetic draping'.

There is not enough observational evidence to support the magnetic draping hypothesis. Past research, instead, was focused on: technological improvements to surveys [Gaensler et al., 2010, 2024; Vanderwoude et al., 2024; Moss et al., 2013; Westmeier, 2018; Taylor et al., 2009; Finkbeiner, 2003; Hutschenreuter and Enßlin, 2020; Hutschenreuter et al., 2022]; the analysis of physical phenomena such as ram pressure stripping [Jones et al., 1996; Grønnow et al., 2017, 2022]; the development of magnetic field derivation techniques [Betti et al., 2019; Grønnow et al., 2017; Mao et al., 2010; Jones et al., 1996; Hill et al., 2013; Schnitzeler, 2010]; and simulations of HVCs [Konz et al., 2002; Grønnow et al., 2017, 2018, 2022; Jung et al., 2022] – all of which lay the groundwork for a proper investigation of magnetic draping.

Previous and recent simulations involve reports produced by Grønnow et al. [2017, 2018, 2022] (henceforth referred to as the “Grønnow et al., simulations”) that provide detailed insight onto how a magnetic draping protects HVCs from collapse, complementing earlier work by Konz et al. [2002]; Jones et al. [1996]. It is shown from the Grønnow et al., simulations that magnetic fields of about 0.3-1 μG can provide stability to HVCs.

However, increasing magnetic field strength beyond a certain threshold can result in less stability; magnetic fields can accelerate the effects of Rayleigh-Taylor (R-T) instabilities and the magnetic pressure applied by the draped fields can also slow down a HVC to the point that it no longer is fast enough to sweep up these magnetic fields. From the Grønnow et al., simulations, the upper threshold where these effects start increasing instability is about 1 μG (specifically stating a maximum of approx. 3 μG), thus HVCs should ideally have a “Goldilocks” magnetic field strength on the order of magnitude of 0.1 μG , with 1 μG being too high, and 0.01 μG being too low.

The effectiveness of magnetic draping is affected by the morphology of these fields and the physical properties of the HVC. The Grønnow et al., simulations state that both the orientation of the magnetic field with respect to the direction of motion of the HVC, and where the magnetic field is located are important considerations. It is expected that HVC is not entirely covered in a magnetic field, only the part that is front facing in the direction of travel. While it is possible to draw conclusions about the survivability of a HVC from the strength of the magnetic field, modelling is required to confirm the accuracy of such conclusions [Betti et al., 2019]. The Grønnow et al., simulations also predict that metallicity can affect the HVC’s survivability, with high-density metal-rich clouds and low-density metal-poor clouds being more unstable than their counterparts.

1.2.2 Faraday Rotation

Magnetic fields cannot directly be imaged by a telescope. Instead, researchers can use the phenomenon of Faraday Rotation to quantify the line-of-sight magnetic field strength. Low-frequency polarised radiation tends to rotate as it travels through a

medium with a magnetic field present. Thus, by recording the stokes parameters of incoming light from distant radio sources, one can derive the Rotation Measure (RM) of incoming radiation, which is a statistical quantifier of Faraday Rotation [Vanderwoude et al., 2024; Brentjens and de Bruyn, 2005].

Vanderwoude et al. [2024] describes the method by which this report's main source, the Polarisation Sky Survey of the Universe's Magnetism (POSSUM), obtained its RMs from raw stokes parameters - which invokes a complex fourier analysis technique to evaluate the rotation measure. There is a direct connection between RM and line-of-sight magnetic field strength, quantified by the below equation [Betti et al., 2019; Vanderwoude et al., 2024; Hill et al., 2013; Kaczmarek et al., 2017; Mao et al., 2010].

$$\text{RM} = 0.812 \int_{s_{\text{observer}}}^{s_{\text{source}}} \frac{n_e(s)}{\text{cm}^{-2}} \frac{B_{\parallel}}{\mu\text{G}} \frac{ds}{\text{pc}} \text{radm}^{-2} \quad (1.1)$$

In which, B_{\parallel} is the magnetic field strength, RM is the Faraday Depth a.k.a. the value of the RM¹, and n_e is the electron density of the medium as a function of line-of-sight distance s . The analysis of this equation, its solutions, and the use of it in calculating the magnitude of draped magnetic fields is discussed in section 4.

Faraday Rotation also occurs in the ISM, due to the slight magnetisation of the ISM [Ferrière, 2001; Mao et al., 2010; Schnitzeler, 2010]. This magnetisation is anti-symmetric with galactic longitude [Mao et al., 2010]. Hence it is also important to remove the foreground from RM observations.

1.2.2.1 Noise Interference

When making radio observations of RMs, a principal factor to consider is signal to noise ratio and detector sensitivity. Radio sources tend to appear in the field after high exposure times as point-like sources. These point-like sources are then collated into an "RM grid" which has a particular density measured in sample points per square degree. The sensitivity of a detector determines the number of source points observed as seen in figure 1.2 [Loi et al., 2019]. At grid densities that are too high, RM sources can bleed into each other, leading to confusion noise. However, no modern radio telescope can reach the confusion limit [Loi et al., 2019].

Signal to noise is of primary concern when measuring the effect of Faraday Rotation. At low enough signal-to-noise ratios, it is possible to encounter 'phantom RMs' which do not accurately represent the real RM [Macquart et al., 2012]. Figure 1.3 gives a visual illustration of this phenomenon. The issue in question is that any observation of RM grids is going to dip below the signal-to-noise threshold of approx. 6, which can introduce an intrinsic scatter in collected RM grid data. There is not much that

¹For the purposes of this report, rotation measure and faraday depth are treated as equivalent, despite their subtle differences

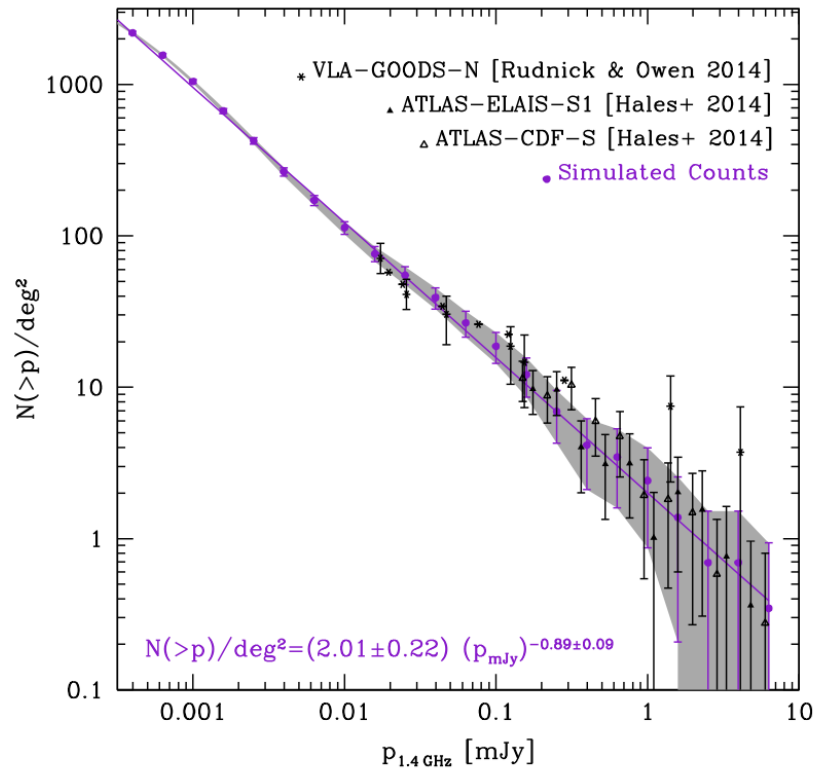


Figure 1.2: From Loi et al. [2019], figure 4. A graph of the relationship between the sensitivity at 1.4 GHz (x-axis) and the minimum number of RM sample points per square degree (y-axis). The black points are not relevant to the report, but the purple line and equation describe the determined relationship.

can be done outside of avoiding regions where the signal-to-noise is likely to be lower (i.e. the Galactic midplane), without modifying the RM grid in a manner that can interfere with its statistical qualities. However, POSSUM itself obtains RM grid data that has signal-to-noise above 8 [Gaensler et al., 2024].

1.3 Smith Cloud

The Smith Cloud is a large HVC that is in the process of colliding with the Galactic disk [Lockman et al., 2008; Tepper-García and Bland-Hawthorn, 2017; Lockman, 2008]. Unlike most HVCs it is quite large in both mass (at least $10^6 M_\odot$ in HI mass) and angular size (the main bulb covering an area of approx. 144 square degrees) [Lockman et al., 2008; Tepper-García and Bland-Hawthorn, 2017; Lockman, 2008]. It has a predicted physical size of 3 square kpc, which is large for a HVC close to the Galactic disk [Lockman et al., 2008]. Due to its proximity and size, the Smith Cloud has been used as a source point of analysis for most of the properties already discussed. For example, metallicity tracers and alpha-group elements in Madsen et al. [2006]; Hill et al. [2009] were determined by analysing the Smith Cloud. Figure 1.4 provides an image of the Smith Cloud in HI from Lockman et al. [2008].

The Smith Cloud has additionally already had its magnetic draping effect analysed. Simulations by Grønnow et al. [2017] and observations by Hill et al. [2013] both agree on an effective magnetic field of $\sim 8 \mu\text{G}$. Note that this number is well above the Goldilocks zone mentioned in section 1.2.1 – indicating the potential exceptionality of the Smith Cloud.

While there are other HVCs that have been sampled in the past, the Smith Cloud has been the main source of HVC information. This is a problem, as the Smith Cloud is an outlier amongst most HVCs – evidenced by its unusual size and magnetic field strength, both factors being related. There is a necessity to analyse more typical nearby HVCs to gain an understanding of the effects of magnetic fields.

1.4 Report Outline and Objectives

The primary objective of this report is to (a) construct a rudimentary algorithm for calculating the effect of magnetic draping in HVCs found in the CGM and halo and, (b) use this base algorithm to come up with a *very* rough estimate for the magnetic field strength surrounding typical HVCs. The primary source of data will be POSSUM, which will be used to obtain the primary outcome of the report. Due to the previous lack of robust RM grid data, along with other periphery data, and a large level of required assumptions, it is not possible to come up with an estimate of field strength for any HVC, that is accurate to within an order of magnitude. The best-case scenario is an estimate that is accurate within a single order of magnitude. Hence, why the

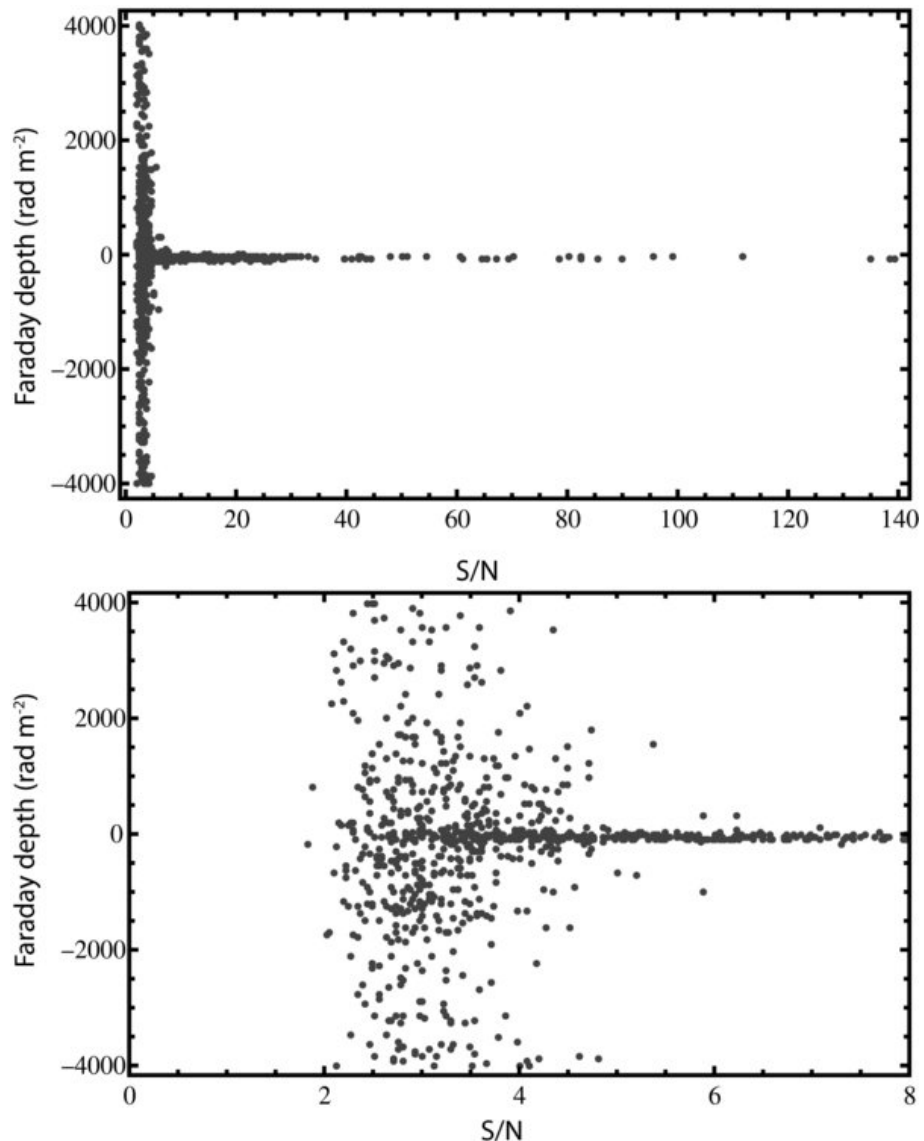


Figure 1.3: From Macquart et al. [2012], figure 1. A graph displaying the effect of observational (stokes parameters) signal-to-noise ratio the resultant faraday depth on a sample set of observations.

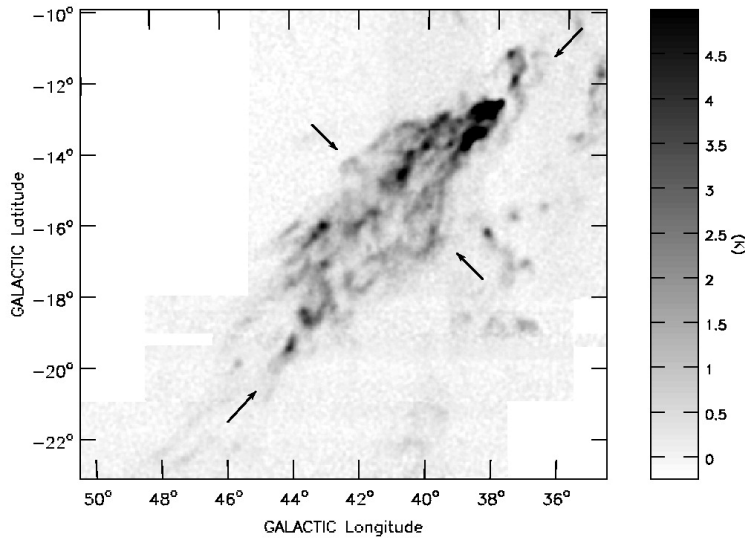


Figure 1.4: From Lockman et al. [2008], figure 1. A HI image of the Smith Cloud taken from the Green Bank Telescope at a local standard of velocity rest of 100 kms^{-1} . The purpose of the arrows are not meaningful to this paper.

aim of this report is to lay the foundations for a future, more detailed analysis, of more numerous HVCs (up to 1693 entries as discussed in section 2.3).

There is a secondary objective that is integral to completing the primary objective: that of foreground removal. Past research, specifically within the analysis of HVCs, has relied on the technique of interpolation to obtain a RM foreground to use in corrections [Schnitzeler, 2010; Moss et al., 2013; Hill et al., 2013]. However, as researchers move onto measurements of magnetism that demand more accuracy, foreground removal needs to equally match that growing need for accuracy – thus this report also aims to investigate avenues for improving foreground subtraction techniques.

This report is split into six sections plus an appendix. Section 2 describes the process of how and which data was obtained to achieve the research question, and how this data was collated together. Section 3 summarises the investigation into foreground removal, which is the secondary aim of the research. Section 4 describes how the magnetic fields for HVCs were derived, and the level to which morphology was involved in the analysis. Section 5 discusses the viability of the methods described in the report, along with broader scientific and statistical considerations. Lastly, section 6 concludes and outlines the many possible directions for future research. Appendix A lists information on how to obtain the program data and algorithms used in research.

Data Collection

To achieve the goals listed in 1.4, several sources of data are required. Furthermore, work needs to be done to collate the data together to measure the magnetic field, quantify the efficacy of foreground removal techniques, and to eliminate problematic data.

2.1 The Australian Square Kilometer Array Pathfinder (ASKAP)

ASKAP represents a recent development in the progress of the field of radio astronomy. It is a part of a new generation of southern-hemisphere telescopes built with the aim to build towards the Square-Kilometer Array (SKA) [Hotan et al., 2021; Gaensler et al., 2010, 2024]. ASKAP aims to allow for the progression of research in the “Pre-SKA” era. As mentioned in section 1.4, the importance of preliminary research in the Pre-SKA era is meant to allow for a more efficient process of astronomy in the coming years when the SKA is fully operational. This means that the data and methodology is simultaneously rudimentary and advanced compared to previous projects.

POSSUM is an ongoing project using ASKAP with the aim of measuring the RM southern sky. The benefit of using ASKAP as opposed to previous RM sky surveys is the RM grid density ASKAP can provide [Gaensler et al., 2010, 2024; Hotan et al., 2021]. Previous surveys such as the NRAO VLA Sky Survey (NVSS) were only able to record an RM grid density of 1 sampling point per square degree, with POSSUM providing a density 30 times greater [Vanderwoude et al., 2024; Gaensler et al., 2010, 2024; Hotan et al., 2021; Taylor et al., 2009]. The higher grid density allows for the analysis of regular-sized HVCs in the CGM, as opposed to only the largest HVCs like the Smith Cloud.

Additionally, POSSUM is set to cover a region of the southern sky that has seldom been recorded properly in previous RM grid surveys, primarily due to the lack of RM radio astronomy in the southern sky [Hutschenreuter and Enßlin, 2020; Hutschenreuter et al., 2022; Gaensler et al., 2010, 2024]. This allows for the analysis of HVCs which otherwise would not be analysed under legacy data.

Generally, Gaensler et al. [2010, 2024] are the references for current POSSUM data. All POSSUM data is recorded using the ASKAP radio frequency band 1 at 880-1088



Figure 2.1: An Aitoff projection of all portions of the RM sky observed by ASKAP for the POSSUM survey. The map is up to date as of May 2024 and all RMs in this map are used in the production of this report. The faraday depth of these RMs are indicated by colour.

MHz [Vanderwoude et al., 2024; Gaensler et al., 2010, 2024]. The POSSUM grid data used in this report represents all collected and processed RMs by the POSSUM survey as of May 2024, with a total RM source count of 188842. Figure 2.1 represents the entire sample on an Aitoff projection.

2.2 Observational Data

While the primary source of data used was from POSSUM, several other sources of data were employed in the process of analysis.

2.2.1 RM Sky Interpolation

The process of estimating RM foreground contributions typically requires the use of an interpolation between RM grid point measurements. While more modern research has been done in interpolating the POSSUM data set, for example the recent paper by Khadir et al. [2024], due to POSSUM's lack of complete sky coverage, it was determined as better to use a whole-sky RM interpolation - this is due to: the uniformity of the map across the whole sky; the level of sky coverage (especially required for section 3); the reliability of using well-developed data; the accuracy of an interpolation of a complete RM sky. The most recent RM sky interpolation came from Hutschenreuter and Enßlin [2020]; Hutschenreuter et al. [2022], which combined all previous sources

of RM grid data with free-free emission from the Planck survey. This survey will be referred to as the “Hutschenreuter map”. Most notably, the Hutschenreuter map has a large ‘blind spot’ near the terrestrial southern pole, with the use of free-free emission to constrain the data better [Hutschenreuter and Enßlin, 2020; Hutschenreuter et al., 2022]. This does not disqualify the merits of using Hutschenreuter map, but should encourage further research into improvements on existing interpolations of the RM sky.

2.2.2 Other Data Sources

Both HI and H-alpha maps of the sky were obtained in the process of data collection. Both maps were used in previous literature to detect HVCs and construct interpolations of the RM sky. In this report specifically, their primary purpose in including them in the collated data is due to illustrative and future application purposes.

The HI sky was taken from the HI4PI 21 cm survey, with modifications done by Westmeier [2018] to filter for high-velocity HI sources (above a column density of $2 \times 10^{18} \text{ cm}^{-2}$). This modification allows for the better detection of HVCs in the sky, however it eliminates the ability for RMs to directly be analysed using the real HI column density, due to the removal of low-velocity modes – a factor which will be accounted for in section 4. Unlike all other sources of data, Westmeier [2018] does not provide uncertainties for its HI emissions. It is assumed that the HI uncertainty is approximately equivalent to the Poisson noise i.e. the logarithmic column density is multiplied by one half.

The H-alpha sky was taken from Finkbeiner [2003], which was a collage of three smaller H-alpha surveys. Unfortunately, this map is also limited by the same problems as the Hutschenreuter map, with a notable lack of coverage near the terrestrial south pole. It was decided that the H-alpha map would be included in the process of collation for the purposes of future research potential.

Both maps, the Hutschenreuter map, and their respective error maps are displayed in figure 2.2. The only exception being the HI error, which is only altered by a scalar. All data sources collected were first converted to a FITS file under the cartesian projection. The location of individual point-values will not be affected by a cartesian projection, however it can introduce distortions at a high galactic latitude. This does need to be accounted for.

2.3 Selection of HVCs

All HVC data was obtained from Moss et al. [2013] (hereafter referred to as the “Moss catalogue”) – a catalogue of all HVCs found using the Galactic All Sky Survey (GASS). The Moss catalogue is a primary source of data, for the location and size analysis of



Figure 2.2: Cartesian plots of peripheral data maps (left): the HI sky from the Westmeier [2018] modification of the HI4PI survey (top); the H-alpha sky from Finkbeiner [2003] (middle); and the Hutschenreuter map from Hutschenreuter and Enßlin [2020]; Hutschenreuter et al. [2022] (bottom). Uncertainty maps for H-alpha and the Hutschenreuter map are displayed respectively (right). The HI uncertainty is not displayed due to it simply being a scalar multiple of the HI map.

HVCs.

The Moss catalogue includes a total of 1693 HVCs, of which most are not viable candidates for analysis. There are several reasons why a particular HVC may introduce significant analysis errors. The first consideration is size. From section 1.1, HVCs globally have incredibly variable sizes, but locally HVCs in the halo are more consistent in size. Exceptions to this rule cannot be included in HVC analysis as they may not be representative of a typical HVC. For example, the Smith Cloud, due to its size, has an abnormally large corresponding magnetic field. Thus, HVCs that were not in an angular size range of $(1, \pi)$ degrees were masked out. The lower limit exists to guarantee that there are enough RMs covering the cloud itself. This reduces the sample to 151 HVCs.

Other considerations made when filtering HVCs were their overlap with the current POSSUM RM grids. Not every HVC is properly covered by the current RM grid. HVCs were filtered out if their centres (obtained from the Moss catalogue) were more than one degree separated from the nearest RM sampling point. This further reduced the sample size to 26 HVCs.

There is a major increase in scatter with POSSUM RMs and interpolated RMs closer to the galactic midplane [Schnitzeler, 2010]. This is explored in later sections; however, figure 2.3 represents this scatter. Because of this, HVCs close to the galactic midplane must be eliminated to reduce scatter – specifically HVCs located with Galactic Latitudes $|b| < 20^\circ$ were excluded. This reduces the sample size to 15.

Lastly, the distortions introduced by cartesian projections need to be accounted for. HVCs located at Galactic Latitudes $|b| > 80^\circ$ were also eliminated from the sample set. This removes one HVC to give a sample size of 14.

2.4 Data Collation

Once the data was obtained, calculations were done using the `astropy.wcs` pipeline. For every RM point in the sky, the estimated foreground RM from the Hutschenreuter map, the HI column density, and the H-alpha flux, including all associated errors were attached to that particular RM sampling point.

2.4.1 HVC Image Overlays

For each HVC, the HI, H-alpha, Hutschenreuter map, and RM grid was ‘cropped’ according to a field twice the size of the maximum HVC source x and y extents. This is to allow for analysis of both RMs in the HVC and surrounding the HVC.

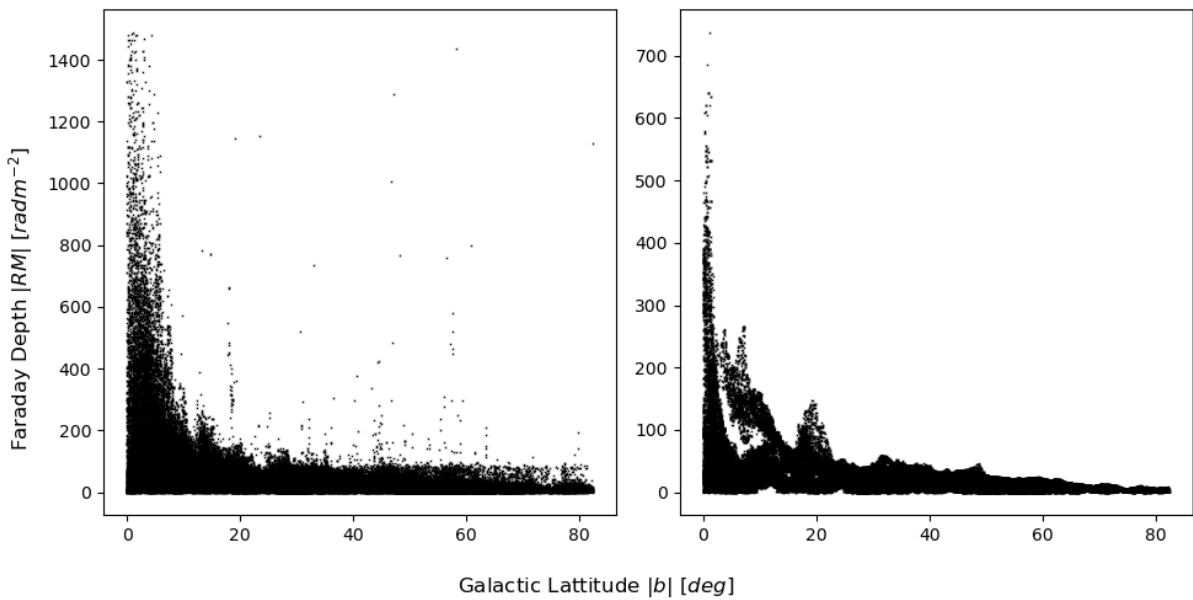


Figure 2.3: (Left) A graph of all ~ 180000 RMs plotted against their corresponding galactic latitude; (Right) The corresponding graph of all interpolated faraday depths matched to the POSSUM RMs. Both graphs represent a significant level of scatter present in RMs collected near the galactic midplane.

Foreground Subtraction

Foreground subtraction remains an open question in the field of RM radio astronomy. Due to the inherent magnetisation of the Galactic halo and the ISM, as discussed in sections 1.2.1 and 1.2.2, there are significant contributions to observed RMs from the Galactic foreground across the entire sky. To correctly determine the magnetic field surrounding objects of interest, one must first remove this source of systematic error.

A prime example of the consequences of not correctly accounting for foreground RM contributions is the paper by McClure-Griffiths et al. [2010], which attempted to estimate the magnetic field strength surrounding HVCs in the Leading Arm. However, as from Jung et al. [2021], this result is possibly erroneous due to the obstruction of the nearby Antila supernova remnant region. While the analysis of multiple HVCs is more likely to prevent these errors from compounding to invalidate the conclusions of the report, it is still useful to account for these contributions as much as possible.

3.1 Interpolation

All previous work on magnetic field analysis of HVCs involve the use of interpolation [Moss et al., 2013; Betti et al., 2019; Westmeier, 2018; Hill et al., 2013]. Interpolations are very beneficial due to its ability to convert a discrete distribution of RM grid points into a continuous distribution of the RM sky. Interpolations also benefit from a ‘smoothing’ effect; that interpolated maps can smooth out small-scale imperfections in the RM grid that may not correspond to actual foreground objects [Hutschenreuter and Enßlin, 2020; Hutschenreuter et al., 2022; Khadir et al., 2024]. This smoothing can occur because of the interpolation algorithm itself, or the lack of RM grid density to resolve objects on a particular scale.

The primary issue with interpolation is that they are too effective a technique at reconstructing the RM foreground. Despite the smoothing effects that they can provide, there is no way one can confirm that the RM sky has not included objects of interest as well; in other words, an interpolated RM sky could contain the profiles of objects of interest. This has the effect of making interpolated maps sourced from high-density RM grids redundant, as the original intention of interpolation is to subtract out foreground contributors to RMs – not the objects of interest themselves.

Thus, with the increased RM grid density afforded by the POSSUM survey, and

future SKA-era projects, it is of high importance that discussions on how to account for these issues can be solved.

3.2 Annulus Subtraction

The immediate alternative is annulus subtraction. This is a method employed across all fields of astronomy, including radio astronomy, being most applicable to single-object analysis. The method generally involves selecting a series of RM sampling points surrounding any given central RM grid point, averaging the selected RMs, and subtracting the average from the central RM grid point.

There are two sub-methods to consider when performing annulus subtraction: fixed-size annulus subtraction and fixed-sampling annulus subtraction. Fixed-size annulus subtraction involves defining an annulus with a constant inner and outer radius and averaging the RMs exclusively within this radial range. Fixed-sampling annulus subtraction involves defining an inner radius and then selecting a fixed amount of RM grid points that are closest to the central point, but still outside the inner radius. Assuming a constant grid density everywhere in the field, a relationship between the two methods can be quantified, as in the following equation:

$$\begin{aligned} R &= \sqrt{r^2 + \frac{N}{\pi n}} \\ N &= \pi n (R^2 - r^2) \end{aligned} \tag{3.1}$$

Where n is the RM grid density in deg^{-2} , r is the inner radius of the annulus in degrees, R is the outer radius of the annulus in degrees (which is directly fixed under the fixed-size regime), and N is the number of RM grid points used (which is directly fixed under the fixed-sampling regime) and is unitless. This means that under a constant RM grid density, these two methods should be approximately equivalent.

There are benefits to both methods. On one hand, fixed-size methods can be described mathematically as convolutions, making them linear. However, they can run into measurement and calculation errors when there is a low amount of RM grid points surrounding the central RM. On the other hand, fixed-sampling methods guarantee a consistent uncertainty and the existence of an average. However, this method is both non-linear and prone to including RM grid points very far away from the central point.

The primary issue with annulus subtraction is determining the size of the annulus, or the amount of RM sampling points to select i.e. what counts as the “foreground”. This issue is what leads to many of the above-mentioned errors in both methods. The logical response is either to select a large annulus that completely removes the objects’



Figure 3.1: An Aitoff projection of all portions of the RM sky observed by ASKAP for the POSSUM survey similar to 2.1, filtered through a proprietary fixed-sampling algorithm with inner radius of $0.4''$ and a sampling constant of 50.

RM contributions (in the case of HVCs this would correspond to an annulus of $1 - \pi$ degrees in radius), or to select a small radius with numerous RM points to capture the foreground contributions both overlapping the object and isolated in the field. Both methods will be analysed in this paper, with the former being discussed in section 3.3.3 and the latter being shown in figure 3.1¹. The specific choice of parameters in the latter method being an inner radius of $0.4''$ and a sample size of 50 grid points – corresponding to an outer radius of approx. 0.728° .

3.3 Fast Fourier Transforms (FFTs)

Many of the methods for foreground subtraction beyond interpolation appear to have a common intersection point in the form of image-based signal processing. Thus, the introduction of Fourier Transforms (FTs) may be a very useful direction for analysis. The benefit of FTs is their linearity, which has several benefits including: the trivialisation uncertainty calculations (quantified in equation 3.3); the linear combination of several kernel techniques; signal processing in separate orthogonal dimensions; and consistent scaling relationships. FTs also can utilise both convolutional blurring and bandpassing separately, with convolutions already being discussed with annulus subtractions.

FFTs extend the benefits of FTs by providing a FT algorithm of $O(N \log N)$ com-

¹The fixed-sampling annulus subtraction was proprietary data collected from the supervisor. However, the quantitative and qualitative analysis of the viability of this method is my own work.

plexity and allowing FTs to be performed over discrete sets of data. This allows for the analysis of high-definition pixellated images, which is not unlike the standard format and use-case of a FITS file, especially when using a cartesian projection of the sky. Thus, by applying 2-dimensional FFTs to provided interpolated RM sky images, it is possible to solve the problem introduced by interpolated high-density RM grids.

3.3.1 Non-Uniform Fast Fourier Transforms (NUFFTs)

FFTs can further be extended to the analysis of non-uniform data sets. Standard FFTs rely on the assumption that the grid of sampling points is uniform, and resultantly output uniform-density frequency distributions. NUFFTs do not require the assumption of uniformity, nor do they need to output uniform-density frequency distributions [Bagchi and Mitra, 1996; Greengard and Lee, 2004]. This means that instead of relying on interpolations at all, FTs can be applied directly to the RM grid itself. The primary sources for NUFFTs used in this paper are Bagchi and Mitra [1996]; Greengard and Lee [2004], with heavy reliance on the python module PyNUFFT (see appendix D for more).

There are three types of NUFFT: Forward, Adjoint, and "True"². The forward and adjoint types are inverses of each other – forward NUFFTs take a uniform image and a set of sampling points and return a non-uniform frequency distribution and adjoint NUFFTs reverses that process. True NUFFTs take a non-uniform distribution and output a non-uniform frequency distribution. True NUFFTs are not generally useful for the purposes of this report.

Applying a forward and then an adjoint NUFFT to a set of RM grid sampling points should perform the same task as creating an interpolation. From there, the intermediary step of a bandpass or kernel can be applied to the frequency distribution to produce an interpolation with objects of a particular scale removed from the field.

The important first step in determining if this method can create a reliable interpolation on its own. First, an image was selected, specifically a grayscale and cropped image of the Cosmic Microwave Background (CMB) from the Planck mission (see appendix C for more). This was chosen as the test image due to the CMB being able to replicate a noisy and 'blobby' structure, the CMB has also been analysed using FFTs for unrelated cosmological purposes.

Then, a random set of sampling points were selected and treated as the 'mock RMs', with the colour of the background corresponding to the intensity of the RM at that point. The image and the sampling points were then given to the PyNUFFT module and transformed in and out of the frequency domain. Figure 3.2 represents the outcomes of this analysis, performed on a sample of simulated RM grids with

²There is no generally accepted nomenclature for type 3 NUFFTs that align with the single-adjective terminology. So "True" is used because it is an accurate descriptor for the type, involving both non-uniform x and k spaces.



Figure 3.2: (Right) A cropped and grayscale image of the CMB. (Left) The same image after being fed through a forward then adjoint NUFFT. The amount of sample points total to 27000. Both plots share a common intensity colourbar for reference.

size $30^\circ \times 30^\circ$. Ignoring the grid-like structure in the recreated image (a consequence of the random point generation algorithm), even with a very high sampling point density or large field, the image is still very low-quality.

This does not disqualify the NUFFT as an analysis technique. Instead, it means that this technique can only work on a very large continuously connected RM set i.e. a complete or partially complete RM grid map of the sky. However, due to the lack of POSSUM data in its early stages, this is a method that must be investigated in the future.

3.3.2 Bandpass Filtering

A simpler method is to directly alter the Hutschenreuter map itself using normal FFTs. First, a 2-D FFT was applied to the Hutschenreuter map. A crosshatch-shaped bandpass was created. This crosshatch imitates a bandpass commonly applied to 1-dimensional signals, where objects of a particular angular size are eliminated by removing all frequencies corresponding to that angular size in the k-space. The equation below quantifies the relationship between frequency and angular size:

$$k_{\text{HVC}} = \frac{1}{2\theta_{\text{HVC}}R} \quad (3.2)$$

Where k_{HVC} is the spatial frequency in deg^{-1} , θ_{HVC} is the angular size of the HVC in degrees, and R is the pixel resolution of the axis, in pixels per degree. Assuming all RM sky images exist in a 2:1 cartesian space, due to the range of galactic latitude and longitude, the value of R is constant across the two axes.

The crosshatch is shaped such that, when multiplied by the original k-space, objects of a particular size are either eliminated or reduced in prevalence. This method



Figure 3.3: Crosshatch-Bandpassed versions of the interpolated RM sky at various opacity gradings - where "original" means 0% opacity. The term "opacity" refers to the effect of the bandpass e.g. 100% opacity means the bandpass completely removes selected frequencies and 50% opacity means that the bandpass halves the presence of selected frequencies.

also guarantees the linearity of the crosshatch 'function'. After this, the inverse FFT is applied to give a resulting foreground map, seen in figure 3.3.

However, bandpassing introduces ripples into the Hutschenreuter map. This effect is expected but undesirable. There are two methods to remove this: either to apply the crosshatch at a certain 'opacity' i.e. the crosshatch is not eliminating all the k-space in its region, but instead is reducing those frequencies by a percentage; or using a more complex window than a Top Hat, such as a Tukey window or Gaussian window. The effects of the former are seen in figure 3.3. The latter was not investigated due to time constraints.

When applying FTs to any interpolated image, it is important to maintain the corresponding uncertainty map's accuracy. This is where one can take advantage of linearity. The following formula below determines how uncertainties can be calculated:

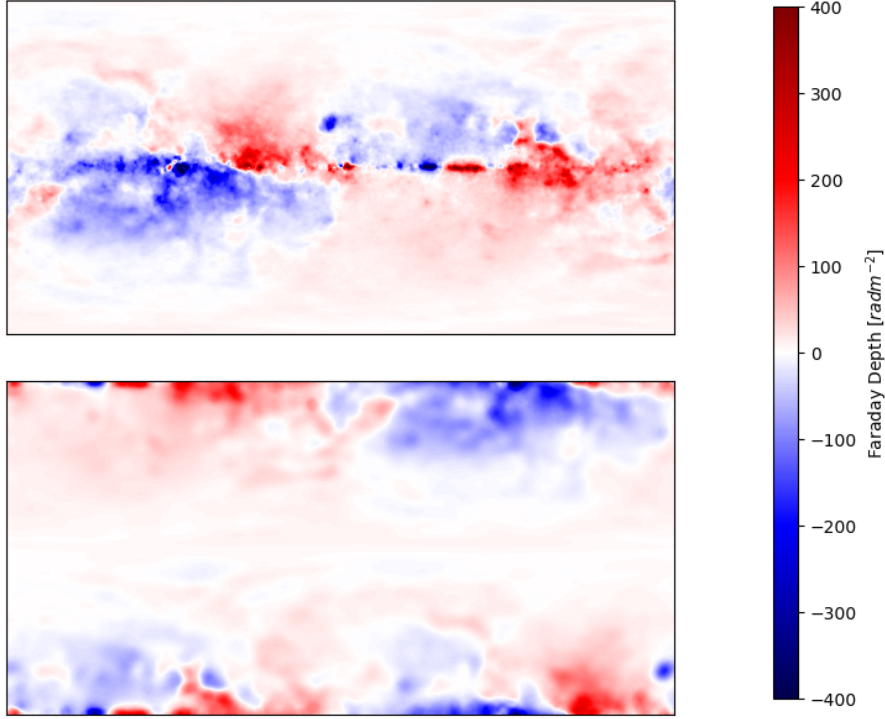


Figure 3.4: Cartesian plots of the interpolated RM sky (Top) compared against the Annulus-Bandpassed version of the interpolated RM sky (Bottom). The annulus kernel used sums to unity, making it act like a unitary operator, standard for blurring techniques [Pulfer, 2019].

$$\sigma_{\text{output}} = \mathfrak{F}^{-1} \left[B(\mathfrak{F}[\sigma_{\text{original}}]) \right] \quad (3.3)$$

Where $B: \sigma \rightarrow \sigma$ is the bandpass function, σ_{output} and σ_{original} is the uncertainty images for the output and input respectively in rad m^{-2} , and \mathfrak{F} is the FT.

3.3.3 Kernel Filtering

The same techniques from above can be applied to convolutions, where the aim is to convolve the Hutschenreuter map with a defined kernel. Two-dimensional convolutions have a time complexity of $O(n^4)$, depending on the kernel size, whereas the FFT has a complexity $O(n^2 \log^2 n)$. By performing a FFT on both the kernel and the Hutschenreuter map separately, then multiplying the two k-spaces together, and applying an inverse FFT, the result is a faster application of a convolution with a kernel. This was the chosen method to demonstrate the large fixed-size annulus subtraction method. Figure 3.4 displays the results of this method.

The main problem, as apparent from this method, is that the annulus kernel acts

as an edge detection algorithm [Pulfer, 2019]. This causes defects at higher absolute galactic latitudes due to the effect of distortions from the cartesian distribution. Another problem is that this subtraction method is being applied to the Hutschenreuter map, instead of the actual RM grid. This secondary issue can be solved by relying on the NUFFT of a larger RM grid. As it stands, this method appears to be incompatible with the goals of foreground removal.

3.4 Characterising the RM data

As seen from figures 1.3 and 2.3, there are several ways in which the RM grid can have ‘bad data’ – most notably in a lack of signal-to-noise and the inherent scatter when observing near the Galactic midplane. Thus, the final step of this chapter is to both characterise the RM sample set and to compare the subtraction methods against each other.

Figure 3.5 represents a simple residual histogram comparison between all the methods discussed in this chapter. The desired result is seen in the residuals between the interpolated or crosshatch-bandpassed RMs and the actual RMs - appearing as a normal distribution centred at zero. This is opposed to the two annulus methods, which do not appear to interact with the RM grid in a desirable manner.

Figure 3.6 demonstrates the similarities between the crosshatch-bandpass and unaltered Hutschenreuter map, with them being related to each other in a linear manner, specifically with a gradient of approximately unity. This is ideal, as it means that the crosshatch-bandpass method is not deviating significantly from the Hutschenreuter map, only altering it subtly. The figure also demonstrates how scattered the RMs become near the Galactic midplane, hence it being plotted for colour to delineate between RMs near and far away from the midplane.

Figure 3.6 also compares the unaltered Hutschenreuter map with the annulus-convolved method (a.k.a. the fixed-sampling annulus method). There is a somewhat linear relationship between the actual RMs and the annulus-convolved RMs, ignoring the heavy scatter closer to the midplane. This gives credibility to this method, and the choice of having a small-sized annulus.

Lastly, figure 3.6 also compares the two annulus methods together. The annulus-bandpass method (a.k.a. the fixed-size annulus method). From the bottom two graphs, the annulus bandpass does not interact properly with the Galactic midplane, sending most RMs to near-zero. Despite this, RMs at higher galactic latitudes ‘blow up’. This implies that the utilised annulus-bandpass method is not a viable for foreground correction.

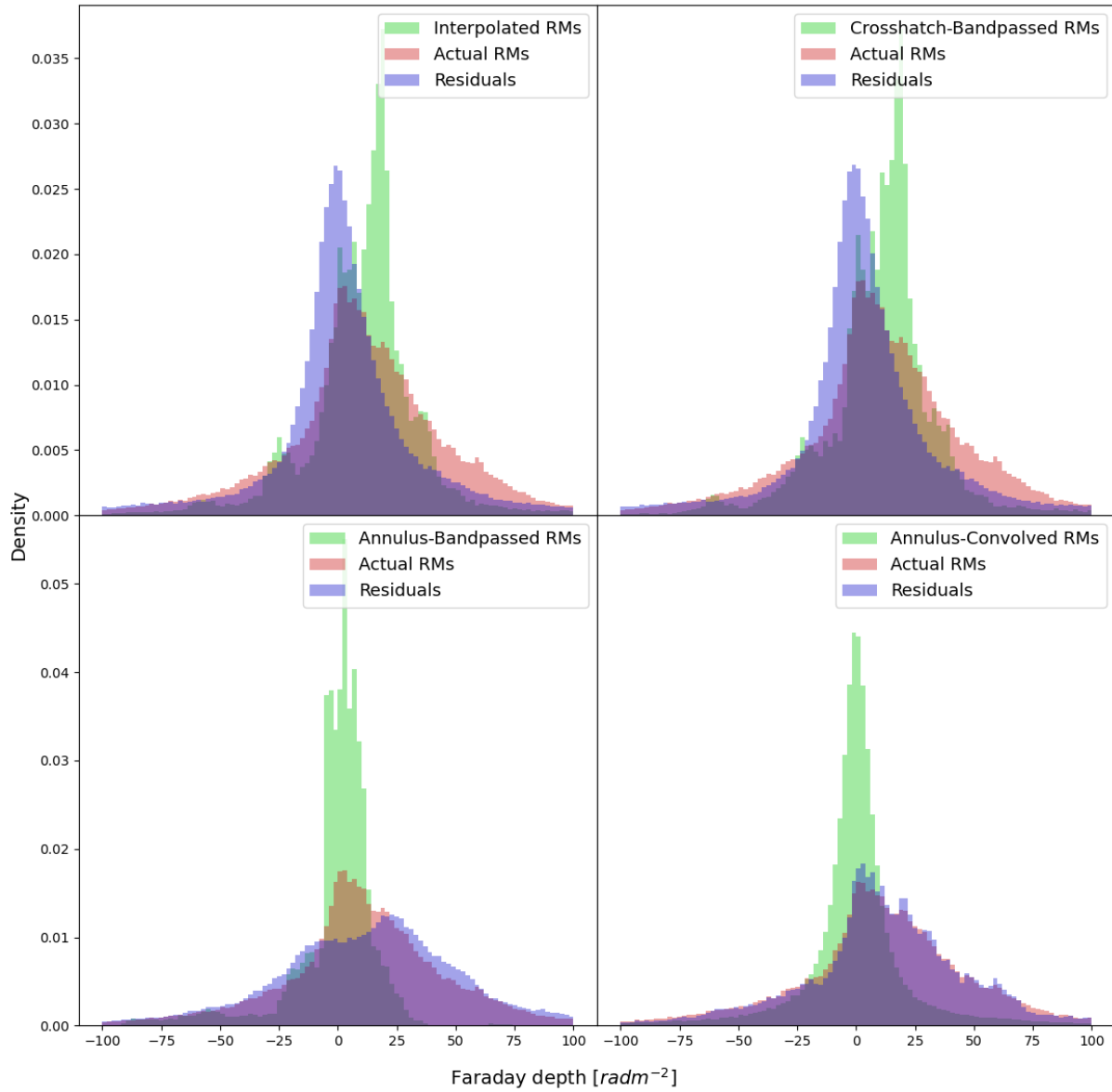


Figure 3.5: Residual histogram plots of the actual POSSUM RMs compared to the corresponding various foreground removal methods: interpolation (Top left); crosshatch-bandpassed (Top right); annulus-bandpassed (Bottom left); and annulus-convolved (Bottom right).

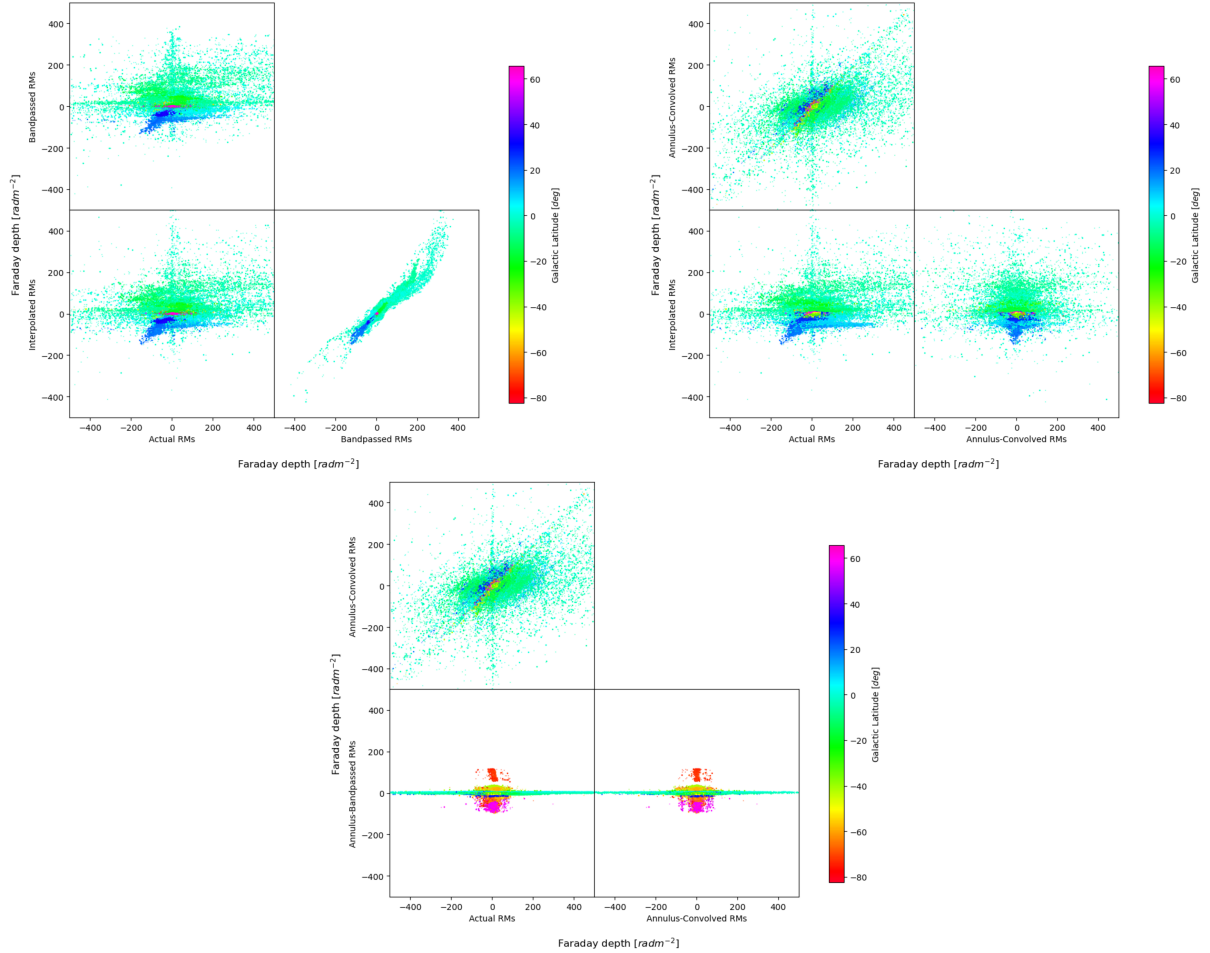


Figure 3.6: Three corner plots of all RM sampling points, describing the relationship between the several associated RM values and Galactic latitude indicated by colour. (Top left) a comparison between actual RMs, interpolated RMs, and Crosshatch-Bandpassed RMs. (Top right) a comparison between actual RMs, interpolated RMs, and Annulus-Convolved RMs. (Bottom) a comparison between actual RMs, Annulus-Bandpassed RMs, and Annulus-Convolved RMs.

3.5 Other Methods

There are other methods for foreground removal that, while researched, were not considered viable options or of enough importance to numerically analyse in this report. However, they may still offer useful methods for future researchers. The first is median filtering, which is like previously discussed convolutional blurring methods. Huang et al. [1979] provides a description of a fast median filtering algorithm for two-dimensional images. Arias-Castro and Donoho [2009] is also a reference describing the potential benefits of median filtering, including a more robust removal of noise due to the statistical properties of the median, and the preservation of edges. It was disregarded in this report due to its inherent non-linearity, and the debatable nature of whether this disadvantage is worth the advantages it can bring. Linear decomposition of line-of-sight RMs are also possible, attempted in Schnitzeler [2010]. However, it is also quite mathematically complex and may not be conducive to a generalised algorithm, hence the lack of focus on this technique in this report.

Magnetic Field Derivation

In constructing a rudimentary algorithm to quantify the effect of magnetic draping on HVCs, as in section 1.4, it is important to pay attention to the validity of the methods being employed and less the accuracy. As an inaccurate methodology can be improved using better data, removing assumptions, and more precision, however an invalid methodology cannot provide a proper estimate whatsoever.

4.1 Assumptions

Due to the significant limitations in available data, the use of assumptions is necessary to begin the process of rough evaluation. Several assumptions were employed in the process of evaluation, some of which are less than satisfactory at contributing an accurate answer to the research question. Again, it is highly important to note that goal is to ensure the validity of the method is sound and to ensure the method's manipulability, but not necessarily provide a guarantee of accuracy and precision.

The first major assumption is that the ionisation fraction of the Galactic halo is approximately constant, i.e. gas in the halo is well-mixed. This does not account for major sources of heterogeneity caused by HVCs (a desired outcome) or other ionised regions such as the Magellanic Clouds (an undesired outcome). It is not necessarily unreasonable to assume this, especially if the region of analysis per HVC is under 4 square degrees.

Simulation data can be used to analyse the problematic nature of assuming a constant ionisation fraction [Grønnow et al., 2017]. However, it is difficult to apply simulation data to observational data due to the sheer variety of analysis capable of being performed by simulations. For now, it is 'good enough' to rely on that assumption from Grønnow et al. [2017] that the ionisation fraction is high and constant.

The second major assumption is that the weighted average of the HI column density surrounding a HVC is linearly proportional to, and biased towards the peak column density in the centre of the HVC. This is an assumption that only works under the consideration of averages, as HI column density is certainly not uniform within clouds, as mentioned in Heitsch et al. [2021]. It also necessitates some level of correlation between line of sight magnetic fields and their uncertainties (a consequence of Poisson noise).

Both above assumptions can, and should, be taken to be unreasonable for providing an accurate estimate of magnetic field strength. However, the result of applying both assumptions is that the line-of-sight magnetic field strength is linearly proportional to the faraday depth with a scaling constant unique to each HVC – as demonstrated in later section 4.2. This greatly simplifies the analysis, without loss of validity, primarily due to the method of calculation explained by Kaczmarek et al. [2017] and in section 4.2.

The third core assumption is that HVCs will appear as approximately circular within the field. Meaning that to distinguish between the surrounding medium and HVC RM grids, a simple circular method can be applied. As seen from the HI plots in figure 4.1, this assumption appears to only be correct in particular cases. But do note that the HI background discriminates for high-VLSR HI emission.

All three assumptions additionally meet the desired goal of an alterable method. As discussed in the discussion and conclusions sections 5.2.2 and 6.1, these three assumptions can be dropped in the presence of more detailed data or more rigorous methodologies manipulated from the one described in this paper.

Lastly, a very typical assumption made is that the RM contribution along a line of sight is averaged across said line of sight. This is not necessarily correct; however, it is a fair assumption that most past literature has made to deconstruct the integral as seen in Kaczmarek et al. [2017]; Moss et al. [2013]; Hill et al. [2013]. This makes the fourth assumption.

4.2 Derivation of Line-of-Sight Magnetic Fields

As from equation 1.1, there is a relationship between the line-of-sight magnetic field and the faraday depth. By removing foreground contributions to the faraday depth, one can isolate the specific contribution of the line-of-sight magnetic field made by the HVC. At the same time, the fourth assumption can be used to solve evaluate the integral, resulting as follows [Hill et al., 2013]:

$$\frac{\langle B_{\parallel} \rangle}{\mu G} = \frac{\langle \Phi_{\text{cor}} \rangle}{0.81 \langle n_e \rangle L_{H^+}} \quad (4.1)$$

Where $\langle B_{\parallel} \rangle$ is the average line-of-sight magnetic field in μG , Φ_{cor} is the corrected faraday depth in radm^{-2} , n_e is the electron density in cm^{-3} , and L_{H^+} is the HVC path length in pc. From this equation, Kaczmarek et al. [2017] derives a simplified equation that eliminates the need to calculate the electron density and path length:

$$\frac{B_{\parallel}}{\mu G} = 3.80 \times 10^{18} \frac{\Phi_{\text{cor}}}{X \langle N_{HI} \rangle} \quad (4.2)$$

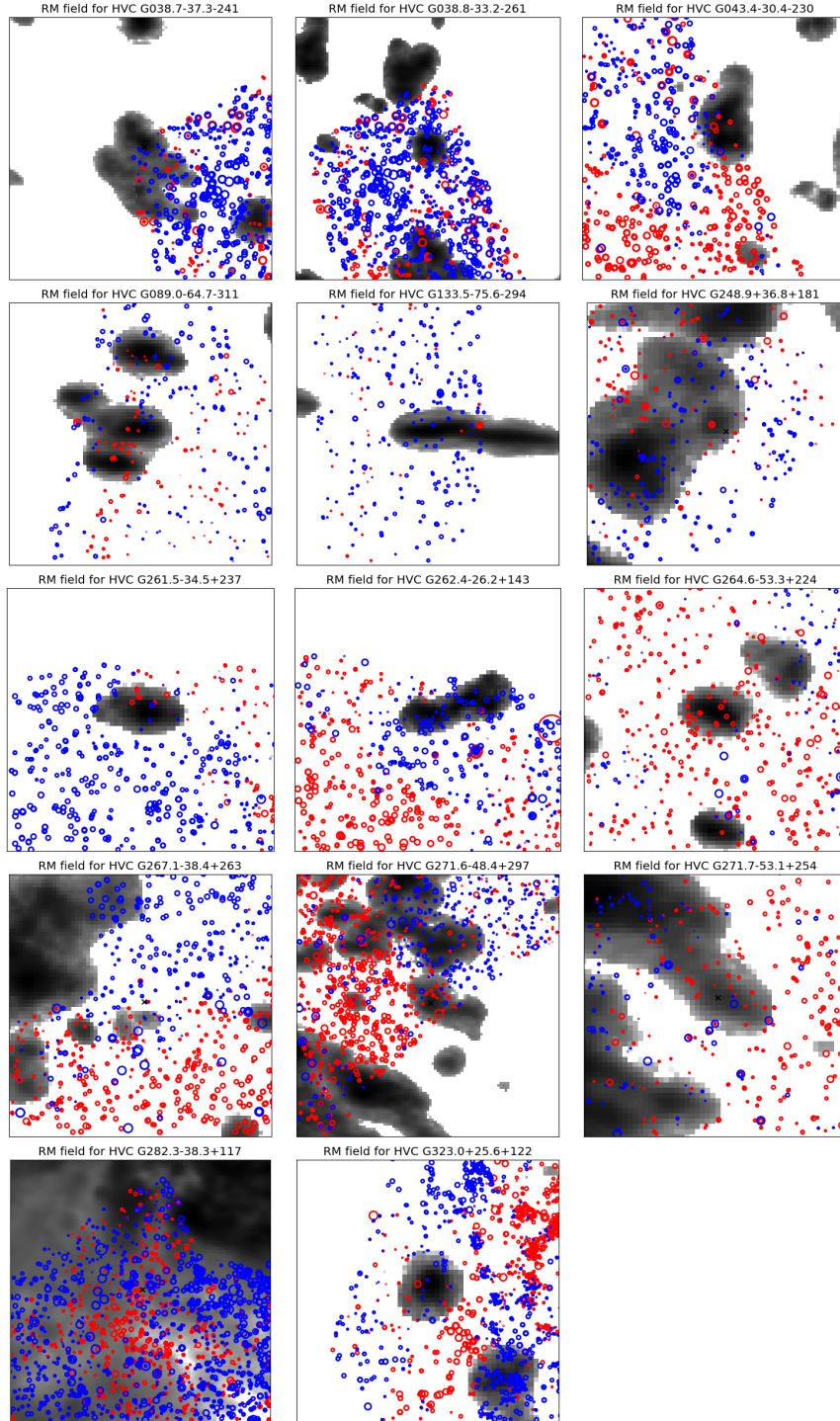


Figure 4.1: All 14 HVCs used in the analysis of the primary outcome. The HI column density is represented using a greyscale image background. The RMs are represented by circular markers, their size equal to the magnitude and the colour representative of their sign with Red being positive. The black circle is the maximum-extent HVC area and the black 'x' indicates the centre of the HVC.

Where X is the unitless ionisation fraction, and $\langle N_{HI} \rangle$ is the weighted average HI column density over the region being analysed, measured in cm^{-2} . This equation can only be derived under the first assumption. Additionally, the use of the average HI column density is intrinsically tied to the second assumption.

Applying both assumptions and utilizing this equation demonstrates that the line-of-sight magnetic field is linearly proportional to the faraday depth. For every RM sampling point, the magnetic field was calculated using this equation. With the assumption that the ionisation fraction is approximately unity, and the average HI column density is equal to the peak HI column density of the HVC. As aforementioned, these values act more as simple placeholders for more detailed analysis, being within an order of magnitude is all that is necessary for the aims of this report.

At this point, it is important to distinguish between what is called 'virtual magnetic field' and 'actual magnetic field'. For any individual RM point source, there are a lot of interferences that may make the resulting magnetic field not representative of the actual magnetic field at that point – more specifically, the turbulent nature of gas mixing in the halo and HVC [Heitsch et al., 2021; Mao et al., 2010; Han and Qiao, 1994]. Thus, calculating the magnetic field value associated with a single RM point source is to be considered 'virtual' – an approximation to the actual magnetic field within a degree of uncertainty. It is only through the statistical analysis of multiple virtual magnetic fields that an actual magnetic field value can be derived. As the combination ensures that turbulence effects are accounted for, due to it being unlikely that random contributions to line-of-sight magnetic fields can become uniform at the point of observation.

Despite the detailed analysis conducted in section 3, it was decided that the non-altered interpolated sky map be used to correct RM contributions. This is due to most already-existing literature relying on this method. From figure 4.2, which displays histograms of the corrected and uncorrected line-of-sight magnetic field points surrounding HVCs. From the figure, it is demonstrated that the Hutschenreuter map can remove the anisotropy of the ISM by turning an uncorrected bimodal symmetric distribution into a normal distribution centred at zero. However, it also is apparent that the correction can introduce a significantly higher variance in the data, shown in the ridge-like structures in figure 4.1, which presents HI images of all 14 HVCs, the overlapping RM grids, and the cropped HI fields. The filtered Moss catalogue, including all 14 HVCs is displayed in appendix B.

4.3 KS Testing

Before evaluating the effect of magnetic draping on HVCs, it is important to first confirm that there is a detectable magnetic field to analyse. To do this, the KS test was employed. The set of RM grid points for each HVC collated in section 2.4.1 include

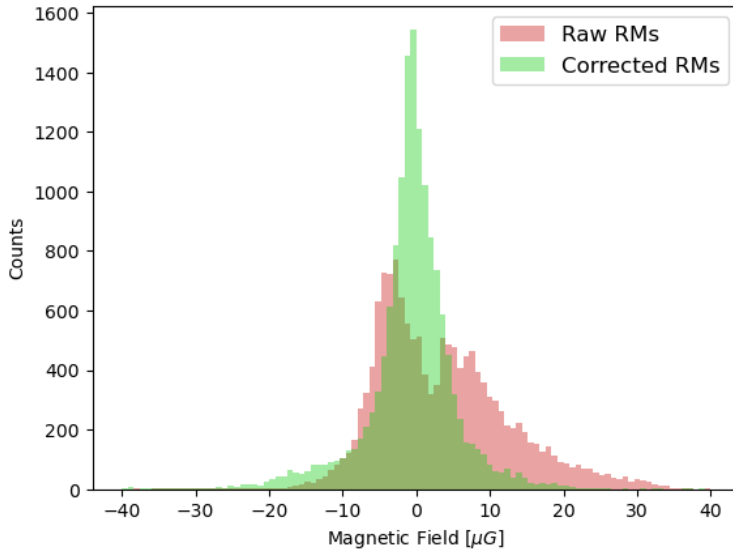


Figure 4.2: Two histograms describing the calculated line-of-sight virtual magnetic field strengths within a certain distance to the 14 sample HVCs. The red histogram uses uncorrected. The green histogram uses corrected RMs.

any grid point within $2 - 2\pi$ degrees of the HVC centre, depending on HVC size. Employing assumption three, two separate populations can be formed by delineating RMs inside and outside a certain circular distance from the HVC centre. The specific radius of delineation was the average value between the Moss catalogue's 'dx' and 'dy' values (i.e. its cartesian dimensions). All sampling points within the defined circle is apart of the "HVC RMs" population, and the ones outside the circle are apart of the "Background RMs" population.

Due to the linear proportionality between the faraday depth and virtual magnetic field, these two values are interchangeable when doing statistical analysis on the individual HVC level. This allows the KS test to be performed on the set of virtual magnetic fields associated with grid points directly, instead of the faraday depth.

A two-sample, two-tailed, KS test was performed comparing both the background and HVC virtual magnetic fields. A critical p-value of 0.001 was assumed to determine if a significant magnetic field was detected. Table 4.1 shows the KS test results applied to each HVC. Out of the 14 HVCs tested, 11 HVCs (79%) had a significant difference between both populations. This is a promising confirmation of the hypothesis presented by the literature, that magnetic draping is an existing phenomenon.

| Name | KS Statistic | p-value |
|-----------------|--------------|----------|
| G038.7-37.3-241 | 0.207 | 3.52E-09 |
| G038.8-33.2-261 | 0.311 | 1.39E-08 |
| G043.4-30.4-230 | 0.241 | 3.61E-11 |
| G089.0-64.7-311 | 0.374 | 1.51E-02 |
| G133.5-75.6-294 | 0.461 | 4.57E-08 |
| G248.9+36.8+181 | 0.081 | 4.53E-01 |
| G261.5-34.5+237 | 0.289 | 5.96E-08 |
| G262.4-26.2+143 | 0.213 | 1.22E-06 |
| G264.6-53.3+224 | 0.32 | 4.07E-05 |
| G267.1-38.4+263 | 0.343 | 2.32E-11 |
| G271.6-48.4+297 | 0.125 | 5.09E-05 |
| G271.7-53.1+254 | 0.227 | 3.40E-04 |
| G282.3-38.3+117 | 0.278 | 8.58E-27 |
| G323.0+25.6+122 | 0.099 | 1.51E-02 |

Table 4.1: A table describing the KS test results for each HVC.

4.4 Mathematical methods to evaluate HVC Magnetic Fields

For the HVCs which did have detectable magnetic fields, the next step is to estimate the strength of the magnetic field draping over each HVC. Previous analyses of the Smith Cloud, such as in Betti et al. [2019]; Hill et al. [2013], utilises a weighted average to determine the magnetic field strength. However, this method may not be transferable to a generalised algorithm. In Betti et al. [2019]; Hill et al. [2013], due to analysing one single and large object, it is possible to divide the object into several smaller sections for analysis. It is not possible to do this especially given the limitations created by assumption three.

While the background virtual magnetic field population will generally follow the expected normal distribution, the in-HVC population can come in multiple varieties including: skewed normal distributions, where the HVC is travelling side-on; bimodal distributions, where the HVC is travelling towards or away from Earth; or sinc distributions - similar to the bimodal distribution, however under the unique case where the HVC magnetic field perfectly overlaps with the corrected background, resulting in a depopulation of virtual magnetic fields where the HVC magnetic field strength should align to. More is provided on these morphologies in section 4.5.

The more complex HVC virtual magnetic field distribution combined with the oversimplified morphology model means that using a weighted average is dubious in validity at best - the same applies to most forms of modal analysis including gaussian

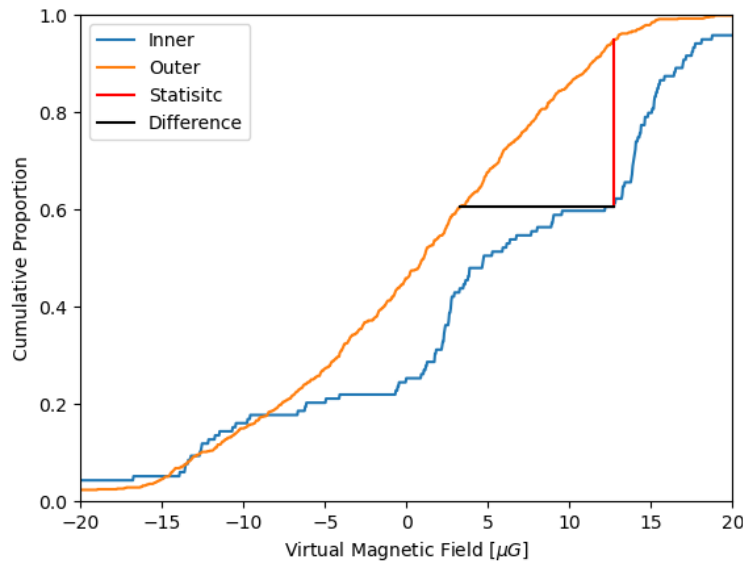


Figure 4.3: A diagram representing the physical evaluation of the KS-EDF method. The graph shows the EDFs of inside and outside populations for an example HVC. The lines drawn on the diagram represent the statistic value and the KS-EDF magnetic field value.

fitting i.e. any method that can not account for antimodal or multimodal analysis. Henceforth, this report proposes two new methods to determine the magnetic field strength surrounding HVCs under the simplified morphological model. Sections 4.4.1 and 4.4.2 attempts to justify the mathematical validity of these two methods, section 4.5 demonstrates validity further through the application of a simple toy model, and section 4.6 shows both the results of using these methods, with some further post-hoc justifications demonstrated in output data.

Regardless of the hypothesis that the weighted average is inadequate, it will still be included as a method in the analysis of both the toy model and actual results, for the point of either disproving or validating said hypothesis.

4.4.1 KS-EDF Method

The first proposed method relies on both the results of the KS test and the Empirical Distribution Functions (EDFs) of the in-HVC and out-HVC populations required to evaluate the KS statistic. The x-axis location of the KS statistic is where the distribution of the two populations differs the greatest. And thus, it is not unreasonable to state that the magnetic field strength corresponds to this location in some manner. This is shown in figure 4.3, where the red line denotes the KS statistic's length and x-axis position.

The second step in this method is to further remove background interference as

explained in section 4.2. This can be done by finding the x-axis location at which the density in the background population EDF equals that of the density of the HVC population EDF at the KS-derived x-axis location. This step has the effect of removing any potential deviation from zero that the magnetic field in the background has due the ridge-like structures, which will appear in the EDF as either (i) any deviation from a standard normal distribution, or (ii) a deviation from the centre of the normal distribution as a function of its uncertainty.

This is shown in figure 4.3 with the black line – the length of the black line representing the final assessed magnetic field value. In this case, the background population in orange is approximately normal. So, case (ii) from the paragraph above is demonstrated.

The second step is not always valid, due to the inherent variability in the EDFs and only being loosely correlated with meaningful population variables. Hence the necessity of further statistical analysis.

4.4.2 Uncertainty Subtraction

A more legitimate method involves the reverse-propagation of uncertainties. An assumption can be made that for some HVCs, there is an inherent variation in the magnetic field as one looks at different locations in the defined morphological circle, appearing as a 'ring' of changing numerical parity. This inherent variance is denoted as σ_{true}^2 .

Additionally, each virtual magnetic field measurement comes with a measurement uncertainty, denoted as $\sigma_{\text{meas.}}$. Propagating these two uncertainties would give what should be the observed variance, σ_{obs}^2 :

$$\sigma_{\text{obs}}^2 = \sigma_{\text{true}}^2 + \sigma_{\text{meas.}}^2. \quad (4.3)$$

The observed uncertainty can be calculated by taking the statistical standard deviation of the population, and the measurement uncertainty can be averaged to give a whole-population measurement uncertainty approximation. This allows for equation 4.3 can be reversed to derive the 'true' variance in the magnetic field:

$$\sigma_{\text{true}} = \sqrt{\text{Var}(B_{\parallel,\text{virt}}) + \langle \sigma_{B_{\parallel,\text{virt}}} \rangle^2} \quad (4.4)$$

By definition of standard deviation, the corresponding true variance can be equivocated to the average separation between virtual magnetic fields in the population, thus quantifying the inherent variation in the HVC magnetic field, i.e. the magnetic field strength.

The same can be done to the background population, instead to detect the potential interferences of the ridge-like structures of the magnetic field. This can be used to

subtract out the background interferences that were included in the derivation of the true in-HVC variance.

A clear potential source of error in this method comes in the fact that the standard deviation is positive, affecting the validity in two separate ways: (i) cases where the average measurement uncertainty is larger than the statistical standard deviation, resulting in a complex uncertainty; (ii) cases where the magnetic field strength *should* be negative but is calculated as positive (before the true background variance is subtracted). Case (i) does not invalidate the method outright but does mean that 'bad data' might have to be thrown out. This happened in only one case as seen in section 4.6. Case (ii) is irrelevant in the conclusion, as the parity of the magnetic field is not a factor being analysed. However, the if the main concern is if the background and HVC true variances differ in sign. This is not of concern because if there is a sign difference, the background ridge-like structures would cancel-out the presence of HVC magnetic fields, resulting in every invalidating occurrence of case (ii) necessarily leading to case (i).

To reiterate, the caveats and assumptions described in this derivation may appear as mathematically or intuitively valid, however it is worthwhile to test things via toy modelling and statistical analysis.

4.5 Toy Model Analysis

E

$$P_{\text{image}}(x, y; k, \alpha, \beta, \gamma) = kP_{\text{background}}(x, y) + P_{\text{HVC}}(x, y; \alpha, \beta, \gamma) \quad (4.5)$$

$$P_{\text{HVC}}(x, y) = \int_{-\infty}^{\infty} R(\alpha, \beta, \gamma) \vec{B}_{\text{sim}}(R^{-1}(\alpha, \beta, \gamma) \cdot (x, y, z)) \cdot \hat{z} dz \quad (4.6)$$

$$\vec{B}_{\text{sim}}(x, y, z) = \begin{cases} \begin{bmatrix} x \\ y \\ z \end{bmatrix} & x \leq 0 \\ \begin{bmatrix} x \\ y \\ z \end{bmatrix} & x > 0 \end{cases} \quad (4.7)$$

4.6 Magnetic Field Results

The results of each method are compiled in table 4.2. Out of 11 HVCs that had detectable magnetic fields, 10 are listed. While HVC G133.5-75.6-294 had a detectable

| Name | Abs. Magnetic Field $ B_{\parallel} $ (μG) | | |
|-----------------|---|-------------------|-------------------|
| | Wgt. Avg. | KS-EDF | σ -Sub. |
| G038.7-37.3-241 | 1.21 ± 0.008 | 2.55 ± 2.182 | 1.20 ± 0.396 |
| G038.8-33.2-261 | 1.14 ± 0.010 | 1.25 ± 1.455 | 0.38 ± 0.325 |
| G043.4-30.4-230 | 1.45 ± 0.007 | 2.28 ± 2.014 | 0.32 ± 0.204 |
| G261.5-34.5+237 | 4.22 ± 0.489 | 7.06 ± 11.798 | 5.89 ± 1.512 |
| G262.4-26.2+143 | 3.85 ± 0.125 | 5.01 ± 7.193 | 11.28 ± 8.325 |
| G264.6-53.3+224 | 1.68 ± 0.162 | 2.12 ± 4.270 | 0.16 ± 1.632 |
| G267.1-38.4+263 | 3.34 ± 0.281 | 9.41 ± 8.558 | 3.76 ± 1.662 |
| G271.6-48.4+297 | 0.09 ± 0.006 | 0.57 ± 2.361 | 0.14 ± 0.303 |
| G271.7-53.1+254 | 0.50 ± 0.100 | 2.39 ± 4.606 | 0.60 ± 1.127 |
| G282.3-38.3+117 | 2.68 ± 0.040 | 3.46 ± 6.279 | 1.97 ± 0.460 |

Table 4.2: A table describing the magnetic field derivations for each HVC. HVCs from the sample of 14 that had no significant KS test detection, or an invalid variance subtraction result are removed.

magnetic field, the variance subtraction method returned a non-real value, indicating that the HVC has ‘bad data’ (as from section 4.4.2 this implies an overestimation of measurement uncertainty).

The distributions of the results are displayed in the boxplots of figure 4.4, which includes the mean (green triangle) and median (orange line) of each set. The Smith Cloud magnetic field as discussed in section 1.3 is marked with a red line, and the upper bound as discussed by the Grønnow et al., simulations in section 1.2.1 is marked in blue. Both values at 8 and 3 μG respectively act as upper bounds for the strength of these HVCs.

From figure 4.4, the magnetic field strengths are overall higher compared to the hypothesised estimate of being on the order of magnitude of 0.1 μG . The three methods appear to visually agree with each other approximately, with the KS-EDF overestimating the magnetic field value, the Variance Subtraction having the greatest spread, and the Weighted Average having the largest tail. It is important to note that due to the logarithmic scale used, the mean is inherently biased to visually appear at higher values. However, the use of a logarithmic scale is still justified due to the order-of-magnitude levels of error.

Figure 4.5 displays the relationship between the calculated magnetic field and the absolute GSR velocity. With all three methods, there appears to be a weak negative correlation in the form of:

$$|V_{\text{GSR}}| \equiv \alpha (|B_{\parallel}| - \beta) \quad (4.8)$$

Table 4.3 states the fitted linear model parameters given by equation 4.8. The

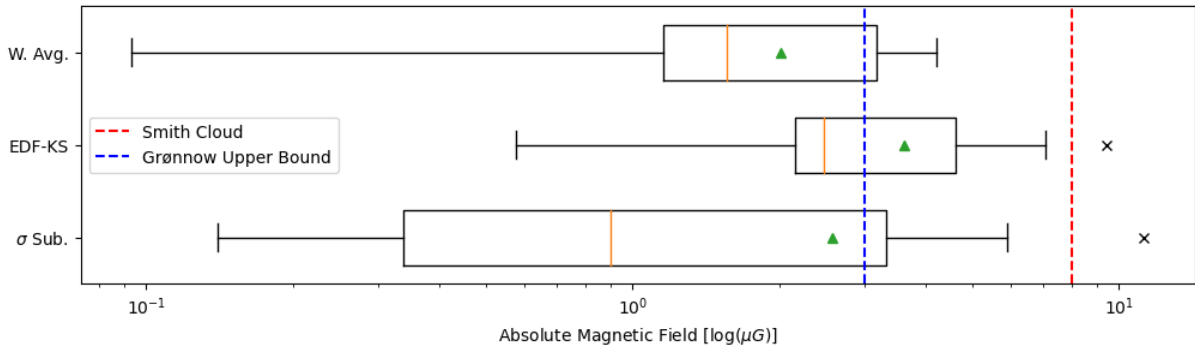


Figure 4.4: A boxplot representing the absolute-value magnetic field of each HVC for both derivational methods. The red and blue dotted lines indicate two upper bounds, one set by the Grønnow et al., simulations, and the other by the Smith Cloud respectively.

| Method | Statistics | | |
|----------------------|--|---|-------------|
| | x-intercept (β) μG | Slope (α) $\text{kms}^{-1}\text{dex}[\mu\text{G}]^{-1}$ | R^2 value |
| Weighted Average | 1.836 | -26.10 | 0.5187 |
| KS-EDF | 2.151 | -34.84 | 0.5715 |
| Variance Subtraction | 2.231 | -17.81 | 0.6320 |

Table 4.3: A table describing the linear fit model parameters of the relationship described in equation 4.8 and displayed in figure 4.5.

R-squared value is used to demonstrate the presence of the weak correlation.

4.6.1 Uncertainties

With each method comes a unique derivation of uncertainties. The uncertainty in the weighted mean is given as trivial – calculated separately for the HVC and background populations, and then propagated.

The uncertainty in the KS-EDF statistic reflects the inherent variability in the method and is calculated by the Euclidean addition of the average measurement uncertainty of both the HVC and background populations. This corresponds to the propagation of virtual magnetic field uncertainties shown in figure 4.3, where the black line is the source of determining the uncertainties to propagate.

The uncertainty in the variance subtraction method was calculated via bootstrap resampling with replacement. The number of samples generated per population is equal to the size of the population being analysed. Once the HVC and background

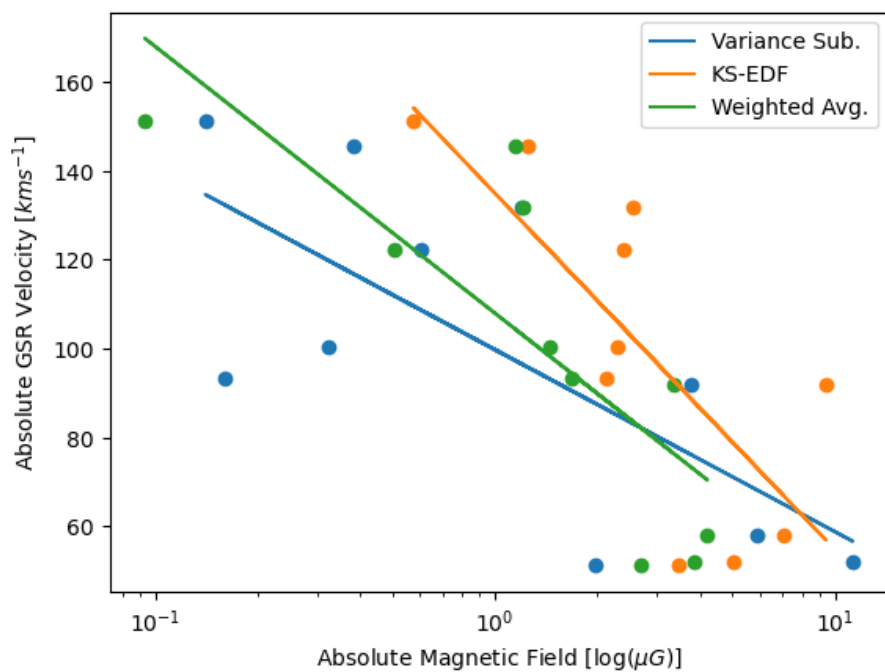


Figure 4.5: A graph displaying the relationship between the absolute GSR velocity and the absolute magnetic field for each corresponding HVC. Lines of fit for the two methods used are displayed as well.

population uncertainties were evaluated, the two uncertainties were propagated to produce the listed result.

4.6.2 Statistical Comparison of Methods

In addition to the reduced chi-squared statistic for the toy model analysis shown in section 4.5, another reduced chi-squared analysis was performed on the magnetic field values calculated for each HVC. The point of comparison is the weighted average. While the hypothesis stated in section 4.4 describes the potential problems with using the weighted average, the distribution in figure 4.4 and the values in table 4.2 demonstrate that the weighted average is still a potentially robust method.

The weighted average has the lowest uncertainties out of the three methods and given its use in previous literature, it was used as the 'expected' value in evaluating the reduced chi-squared statistic. Like the toy model statistical analysis, it was assumed that there were no parameters in the models, because all methods were exclusively mathematically derived from the data.

For the KS-EDF method, the reduced chi-squared statistic was 0.1378, and for the variance subtraction method, it was 14.25. Both values are an order of magnitude away from unity, which mainly demonstrates that the KS-EDF overestimates uncertainties, and additionally the pitfalls of the variance subtraction method. The results of this test does not immediately disqualify either method, but it does provide credence to the hypothesis in section 4.5 that these methods have specific points of failure. It is also important to note that there were only 10 degrees of freedom for these statistics.

Discussion

E

5.1 Foreground Removal

- Edge Detection and Rippling
- Comparison of Methods
- Sample Size Limitations

5.1.1 Edge Detection and Rippling

E

5.1.2 Comparison of Methods

E

5.1.3 Sample Size Limitations

E

5.2 Magnetic Field Derivation

- Data Collection
 - HI and H-alpha Data (Not needed!)
- Neccesity of Assumptions
- Validity of Derivation Methods and VGSR
- Uncertainty Analysis

5.2.1 Data Collection

E

5.2.2 Neccesity of Assumptions

E

5.2.3 Validity of Derivation Methods

E

5.2.4 Uncertainty Analysis

E

Conclusions

E

6.1 Future Research

Also comment on projects in current development. Including Tahani et al. [2024].

Bibliography

- ARIAS-CASTRO, E. AND DONOHO, D. L., (2009). Does median filtering truly preserve edges better than linear filtering? *The Annals of Statistics*, 37(3), 1172–1206. doi:10.1214/08-AOS604. (cited on page 26)
- BAGCHI, S. AND MITRA, S., (1996). The nonuniform discrete fourier transform and its applications in filter design. ii. 2-d. *IEEE Transactions on Circuits and Systems II: Analog and Digital Signal Processing*, 43(6), 434–444. doi:10.1109/82.502316. (cited on page 19)
- BECK, A. M., LESCH, H., DOLAG, K., KOTARBA, H., GENG, A., AND STASYSZYN, F. A., (2012). Origin of strong magnetic fields in milky way-like galactic haloes. *Monthly Notices of the Royal Astronomical Society*, 422(3), 2152–2163. doi:10.1111/j.1365-2966.2012.20759.x. (cited on page 3)
- BETTI, S. K., HILL, A. S., MAO, S. A., GAENSLER, B. M., LOCKMAN, F. J., McCLURE-GRIFFITHS, N. M., AND BENJAMIN, R. A., (2019). Constraining the magnetic field of the smith high-velocity cloud using faraday rotation. *The Astrophysical Journal*, 871(2), 215. doi:10.3847/1538-4357/aaf886. (cited on pages 4, 5, 16, and 32)
- BLAND-HAWTHORN, J. AND MALONEY, P. R., (1999). The galactic halo ionizing field and h alpha distances to hvcs. *arXiv*. doi:10.48550/arXiv.astro-ph/9812297. (cited on page 2)
- BLITZ, L., SPERGEL, D. N., TEUBEN, P. J., HARTMANN, D., AND BURTON, W. B., (1999). High-velocity clouds: Building blocks of the local group. *ApJ*, 514(2), 818. doi:10.1086/306963. (cited on pages 1 and 2)
- BRENTJENS, M. A. AND DE BRUYN, A. G., (2005). Faraday rotation measure synthesis. *Astronomy & Astrophysics*, 441(3), 1217–1228. doi:10.1051/0004-6361:20052990. (cited on page 5)
- DURSI, L. J. AND PFROMMER, C., (2008). Draping of cluster magnetic fields over bullets and bubbles—morphology and dynamic effects. *The Astrophysical Journal*, 677(2), 993. doi:10.1086/529371. (cited on page 3)
- FERRIÈRE, K. M., (2001). The interstellar environment of our galaxy. *Reviews of Modern Physics*, 73(4), 1031–1066. doi:10.1103/RevModPhys.73.1031. (cited on page 5)

-
- FINKBEINER, D. P., (2003). A full-sky $h\alpha$ template for microwave foreground prediction. *The Astrophysical Journal*, 146(2), 407. doi:10.1086/374411. (cited on pages vii, 2, 4, 12, and 13)
- GAENSLER, B. M., HEALD, G. H., McCLURE-GRIFFITHS, N. M., ANDERSON, C. S., ECK, C. L. V., WEST, J. L., THOMSON, A. J. M., LEAHY, J. P., RUDNICK, L., MA, Y. K., AKAHORI, T., GÜRKAN, G., LANDECKER, T. L., MAO, S. A., O'SULLIVAN, S. P., RAJA, W., SUN, X., VERNSTROM, T., BAIDOO, L., CARRETTI, E., TAYLOR, A. R., WILLIS, A., OSINGA, E., LIVINGSTON, J. D., AN, T., BRACCO, A., BRÜGGEN, M., ESWARIAH, C., ENSSLIN, T., UPASANA, G., IDEGUCHI, S., JUNG, S. L., KACZMAREK, J. F., KOTHES, R., LAZAREVIĆ, S., LEAHY, D., LOI, F., PANDHI, A., PRICE, J. M., SHEN, A. X., SETA, A., SOBEY, C., STUARDI, C., AND VELOVIĆ, V., (2024). The polarisation sky survey of the universe's magnetism (possum). i. science goals and survey description. In preperation. (cited on pages 4, 7, 10, and 11)
- GAENSLER, B. M., LANDECKER, T. L., AND TAYLOR, A. R., (2010). Survey science with askap: Polarisation sky survey of the universes's magnetism (possum). In *Bulletin of the American Astronomical Society*. (cited on pages 4, 10, and 11)
- GREENGARD, L. AND LEE, J.-Y., (2004). Accelerating the nonuniform fast fourier transform. *Society for Industrial and Applied Mathematics Reviews*, 46(3), 443–454. doi:10.1137/S003614450343200X. <https://doi.org/10.1137/S003614450343200X>. (cited on page 19)
- GRØNNOW, A., TEPPER-GARCÍA, T., AND BLAND-HAWTHORN, J., (2018). Magnetic fields in the galactic halo restrict fountain-driven recycling and accretion. *The Astrophysical Journal*, 865(1), 64. doi:10.3847/1538-4357/aada0e. (cited on pages 3 and 4)
- GRØNNOW, A., TEPPER-GARCÍA, T., BLAND-HAWTHORN, J., AND FRATERNALI, F., (2022). The role of the halo magnetic field on accretion through high-velocity clouds. *Monthly Notices of the Royal Astronomical Society*, 509(4), 5756–5770. doi:10.1093/mnras/stab3452. (cited on pages 3 and 4)
- GRØNNOW, A., TEPPER-GARCÍA, T., BLAND-HAWTHORN, J., AND McCLURE-GRIFFITHS, N. M., (2017). Magnetized high velocity clouds in the galactic halo: A new distance constraint. *The Astrophysical Journal*, 845(1), 69. doi:10.3847/1538-4357/aa7ed2. (cited on pages ix, 3, 4, 7, 27, 36, and 37)
- HAN, J. L. AND QIAO, G. J., (1994). The magnetic field in the disk of our galaxy. *Astronomy & Astrophysics*, 288, 759–772. <https://ui.adsabs.harvard.edu/abs/1994AnA...288..759H>. (cited on pages 3 and 30)
- HAYAKAWA, T. AND FUKUI, Y., (2024). Dust-to-neutral gas ratio of the intermediate- and high-velocity h i clouds derived based on the sub-mm dust emission for the

-
- whole sky. *Monthly Notices of the Royal Astronomical Society*, 529(1), 1–31. doi:10.1093/mnras/stae302. (cited on page 3)
- HEITSCH, F., MARCHAL, A., MIVILLE-DESCHÈNES, M.-A., SHULL, J. M., AND FOX, A. J., (2021). Mass, morphing, metallicities: the evolution of infalling high velocity clouds. *Monthly Notices of the Royal Astronomical Society*, 509(3), 4515–4531. doi:10.1093/mnras/stab3266. <https://doi.org/10.1093/mnras/stab3266>. (cited on pages 27 and 30)
- HEITSCH, F. AND PUTMAN, M. E., (2009). The fate of high-velocity clouds: Warm or cold cosmic rain? *The Astrophysical Journal*, 698(2), 1485. doi:10.1088/0004-637X/698/2/1485. (cited on page 3)
- HILL, A. S., HAFFNER, L. M., AND REYNOLDS, R. J., (2009). Ionized gas in the smith cloud. *The Astrophysical Journal*, 703(2), 1832. doi:10.1088/0004-637X/703/2/1832. (cited on pages 2, 3, and 7)
- HILL, A. S., MAO, S. A., BENJAMIN, R. A., LOCKMAN, F. J., AND MCCLURE-GRIFFITHS, N. M., (2013). Magnetized gas in the smith high velocity cloud. *The Astrophysical Journal*, 777(1), 55. doi:10.1088/0004-637X/777/1/55. (cited on pages 4, 5, 7, 9, 16, 28, and 32)
- HOTAN, A. W., BUNTON, J. D., CHIPPENDALE, A. P., WHITING, M., TUTHILL, J., MOSS, V. A., McCONNELL, D., AMY, S. W., HUYNH, M. T., ALLISON, J. R., AND ET AL., (2021). Australian square kilometre array pathfinder: I. system description. *Publications of the Astronomical Society of Australia*, 38, e009. doi:10.1017/pasa.2021.1. (cited on page 10)
- HUANG, T., YANG, G., TANG, AND G., (1979). A fast two-dimensional median filtering algorithm. *IEEE Transactions on Acoustics, Speech, and Signal Processing*, 27(1), 13–18. doi:10.1109/TASSP.1979.1163188. (cited on page 26)
- HUTSCHENREUTER, S., ANDERSON, C. S., BETTI, S., BOWER, G. C., BROWN, J.-A., BRÜGGEN, M., CARRETTI, E., CLARKE, T., CLEGG, A., COSTA, A., CROFT, S., ECK, C. V., GAENSLER, B. M., DE GASPERIN, F., HAVERKORN, M., HEALD, G., HULL, C. L. H., *, INOUE, M., JOHNSTON-HOLLITT, M., KACZMAREK, J., LAW, C., MA, Y. K., MACMAHON, D., MAO, S. A., RISELEY, C., ROY, S., SHANAHAN, R., SHIMWELL, T., STIL, J., SOBEY, C., O'SULLIVAN, S. P., TASSE, C., VACCA, V., VERNSTROM, T., WILLIAMS, P. K. G., WRIGHT, M., AND ENSSLIN, T. A., (2022). The galactic faraday rotation sky 2020. *Astronomy & Astrophysics*, 657(A43). doi:10.1051/0004-6361/202140486. (cited on pages vii, 4, 10, 11, 12, 13, and 16)
- HUTSCHENREUTER, S. AND ENSSLIN, T. A., (2020). The galactic faraday depth sky revisited. *Astronomy & Astrophysics*, 633(A150). doi:10.1051/0004-6361/201935479. (cited on pages vii, 4, 10, 11, 12, 13, and 16)

-
- JONES, T. W., RYU, D., AND AND, I. L. T., (1996). The magnetohydrodynamics of supersonic gas clouds: Mhd cosmic bullets and wind-swept clumps. *The Astrophysical Journal*, 473(1), 365. doi:10.1086/178151. (cited on pages 3 and 4)
- JUNG, S. L., GRØNNOW, A., AND MCCLURE-GRIFFITHS, N. M., (2022). Magnetic field draping around clumpy high-velocity clouds in galactic halo. *Monthly Notices of the Royal Astronomical Society*, 522(3), 4161–4180. doi:10.1093/mnras/stad1236. (cited on pages 3 and 4)
- JUNG, S. L., MCCLURE-GRIFFITHS, N. M., AND HILL, A. S., (2021). Distant probes of rotation measure structure: where is the faraday rotation towards the magellanic leading arm? *Monthly Notices of the Royal Astronomical Society*, 508(3), 3921–3935. doi:10.1093/mnras/stab2773. (cited on page 16)
- JUNG, S. L., MCCLURE-GRIFFITHS, N. M., PAKMOR, R., MA, Y. K., HILL, A. S., ECK, C. L. V., AND ANDERSON, C. S., (2023). Sampling the faraday rotation sky of tng50: Imprint of the magnetised circumgalactic medium around milky way-like galaxies. Accepted to MNRAS. (cited on page 3)
- KACZMAREK, J. F., PURCELL, C. R., GAENSLER, B. M., MCCLURE-GRIFFITHS, N. M., AND STEVENS, J., (2017). Detection of a coherent magnetic field in the magellanic bridge through faraday rotation. *Monthly Notices of the Royal Astronomical Society*, 467(2), 1776–1794. doi:10.1093/mnras/stx206. (cited on pages 1, 5, and 28)
- KAWAGUCHI, I., (1952). On the excitation and ionization temperature of the hydrogen in the chromosphere. *Publications of the Astronomical Society of Japan*, 4, 131. (cited on page 3)
- KHADIR, A., PANDHI, A., HUTSCHENREUTER, S., GAENSLER, B. M., VANDERWOUDE, S., WEST, J. L., AND O'SULLIVAN, S. P., (2024). Choosing interpolation techniques for reconstructing galactic faraday rotation. Submitted to ApJ. (cited on pages 11 and 16)
- KONZ, C., BRÜNS, C., AND BIRK, G. T., (2002). Dynamical evolution of high velocity clouds in the intergalactic medium. *Astronomy & Astrophysics*, 391(2), 713–723. doi:10.1051/0004-6361:20020863. (cited on pages vii, 2, 3, and 4)
- LOCKMAN, F. J., (2008). *High-Velocity Clouds Merging with the Milky Way*, chap. 53, 239–242. Springer. ISBN 978-1-4020-6932-1. (cited on page 7)
- LOCKMAN, F. J., BENJAMIN, R. A., HEROUX, A. J., AND LANGSTON, G. I., (2008). The smith cloud: A high-velocity cloud colliding with the milky way. *The Astrophysical Journal*, 679(1), L21. doi:10.1086/588838. (cited on pages vii, 7, and 9)

- LOI, F., MURGIA, M., GOVONI, F., VACCA, V., PRANDONI, I., BONAFEDE, A., AND FERETTI, L., (2019). Simulations of the polarized radio sky and predictions on the confusion limit in polarization for future radio surveys. *Monthly Notices of the Royal Astronomical Society*, 485(4), 5285–5293. doi:10.1093/mnras/stz350. <https://doi.org/10.1093/mnras/stz350>. (cited on pages vii, 5, and 6)
- MACQUART, J.-P., EKERS, R. D., FEAIN, I., AND JOHNSTON-HOLLITT, M., (2012). On the reliability of polarization estimation using rotation measure synthesis. *The Astrophysical Journal*, 750(2), 139. doi:10.1088/0004-637X/750/2/139. <https://dx.doi.org/10.1088/0004-637X/750/2/139>. (cited on pages vii, 5, and 8)
- MADSEN, G. J., REYNOLDS, R. J., AND HAFFNER, L. M., (2006). A multiwavelength optical emission line survey of warm ionized gas in the galaxy. *The Astrophysical Journal*, 652(1), 401. doi:10.1086/508441. (cited on pages 2, 3, and 7)
- MAO, S. A., GAENSLER, B. M., HAVERKORN, M., ZWEIBEL, E. G., MADSEN, G. J., MCCLURE-GRIFFITHS, N. M., SHUKUROV, A., AND KRONBERG, P. P., (2010). A survey of extragalactic faraday rotation at high galactic latitude: The vertical magnetic field of the milky way toward the galactic poles. *The Astrophysical Journal*, 714(2), 1170. doi:10.1088/0004-637X/714/2/1170. (cited on pages 3, 4, 5, and 30)
- MCCLURE-GRIFFITHS, N. M., MADSEN, G. J., GAENSLER, B. M., McCONNELL, D., AND SCHNITZELER, D. H. F. M., (2010). Measurement of a magnetic field in a leading arm high-velocity cloud. *The Astrophysical Journal*, 725(1), 275. doi:10.1088/0004-637X/725/1/275. (cited on pages 1 and 16)
- Moss, V. A., MCCLURE-GRIFFITHS, N. M., MURPHY, T., PISANO, D. J., KUMMERFELD, J. K., AND CURRAN, J. R., (2013). High-velocity clouds in the galactic all sky survey. i. catalog. *The Astrophysical Journal*, 209(1), 12. doi:10.1088/0067-0049/209/1/12. (cited on pages 4, 9, 12, 16, and 28)
- PULFER, E.-M., (2019). *Different Approaches to Blurring Digital Images and Their Effect on Facial Detection*. Honour's thesis, University of Arkansas. (cited on pages viii, 22, and 23)
- PUTMAN, M., PEEK, J., AND JOUNG, M., (2012). Gaseous galaxy halos. *Annual Reviews of Astronomy & Astrophysics*, 50, 491–529. doi:10.1146/annurev-astro-081811-125612. (cited on page 2)
- SCHNITZELER, D. H. F. M., (2010). The latitude dependence of the rotation measures of nvss sources. *Monthly Notices of the Royal Astronomical Society: Letters*, 409(1), L99–L103. doi:10.48550/arXiv.1011.0737. (cited on pages 4, 5, 9, 14, and 26)

- TAHANI, M., NGO, J. M., GLOVER, J., CLAIRMONT, R., ZARAZUA, G. M., AND PLUME, R., (2024). Mc-blos: Determination of the line-of-sight component of magnetic fields associated with molecular clouds. Submitted to ApJ. (cited on page 42)
- TAYLOR, A. R., STIL, J. M., AND SUNSTRUM, C., (2009). A rotation measure image of the sky. *The Astrophysical Journal*, 702(2), 1230. doi:10.1088/0004-637X/702/2/1230. (cited on pages 4 and 10)
- TEPPER-GARCÍA, T. AND BLAND-HAWTHORN, J., (2017). The Smith Cloud: surviving a high-speed transit of the Galactic disc. *Monthly Notices of the Royal Astronomical Society*, 473(4), 5514–5531. doi:10.1093/mnras/stx2680. <https://doi.org/10.1093/mnras/stx2680>. (cited on page 7)
- VANDERWOUDE, S., WEST, J. L., GAENSLER, B. M., RUDNICK, L., VAN ECK, C. L., THOMSON, A. J. M., H.ANDERNACH, ANDERSON, C. S., CARRETTI, E., HEALD, G. H., LEAHY, J. P., MCCLURE-GRIFFITHS, N. M., O'SULLIVAN, S. P., TAHANI, M., AND WILLIS, A. G., (2024). Prototype faraday rotation measure catalogs from the polarization sky survey of the universe's magnetism (possum) pilot observations. Submitted to ApJ. (cited on pages 4, 5, 10, and 11)
- WAKKER, B., (1991). High-velocity clouds. *Symposium - International Astronomical Union*, 144, 27–40. doi:10.1017/S0074180900088884. (cited on pages 1 and 2)
- WAKKER, B. P. AND VAN WOERDEN, H., (1997). High-velocity clouds. *Annual Reviews of Astronomy & Astrophysics*, 35, 217–266. doi:10.1146/annurev.astro.35.1.217. (cited on pages 1 and 2)
- WESTMEIER, T., (2018). A new all-sky map of galactic high-velocity clouds from the 21-cm hi4pi survey. *Monthly Notices of the Royal Astronomical Society*, 474(1), 289–299. doi:10.1093/mnras/stx2757. (cited on pages vii, 2, 4, 12, 13, and 16)

Appendix

A Developed code and data

E

B All HVCs and HVC Calculations

E

C Planck Mission Cosmic Microwave Background

E

D PyNUFFT Python Module

E